Communications Biology

https://doi.org/10.1038/s42003-026-10356-z

Article in Press

FGFR3 oncogenic activation drives oxidative metabolic reprogramming in bladder cancer: a systems metabolomics approach

Received: 5 June 2025

Accepted: 18 May 2026

Cite this article as: Ducci, G., Ciufolini, G., Campioni, G. *et al. FGFR3* oncogenic activation drives oxidative metabolic reprogramming in bladder cancer: a systems metabolomics approach. *Commun Biol* (2026). https://doi.org/10.1038/s42003-026-10356-z

Giacomo Ducci, Giorgia Ciufolini, Gloria Campioni, Valentina Pasquale, Giulia Gigliotti, Simone Ponzetto, Daniele Benedetti, Bruno Giovanni Galuzzi, Deborah D'Aliberti, Silvia Spinelli, Vrunda Satasiya, Elisa Ventura, Chiara Raggi, Riccardo Vago, Marcella Bonanomi, Daniela Gaglio, Antonio Giordano, Andrea Morrione, Chiara Damiani, Rocco Piazza, Daniel Oscar Cicero, Marco Vanoni, Greta Petrella & Elena Sacco

FGFR3 oncogenic activation drives oxidative metabolic reprogramming in bladder cancer: a systems metabolomics approach

Giacomo Ducci [1,2†], Giorgia Ciufolini [3†], Gloria Campioni [1,2], Valentina Pasquale [1,2], Giulia Gigliotti [1,2], Simone Ponzetto[1,2], Daniele Benedetti [1,2], Bruno Giovanni Galuzzi [4], Deborah D'Aliberti [5], Silvia Spinelli [5], Vrunda Satasiya [6,7], Elisa Ventura [6,8], Chiara Raggi [9], Riccardo Vago [8,10], Marcella Bonanomi [2,11], Daniela Gaglio [2,11], Antonio Giordano [6,7], Andrea Morrione [6], Chiara Damiani[1,2], Rocco Piazza [5], Daniel Oscar Cicero [3], Marco Vanoni [1,2***], Greta Petrella [3‡**] and Elena Sacco [1,2‡*]

[1] Department of Biotechnology and Biosciences, University of Milano-Bicocca, Piazza della Scienza 2, 20126 Milan, Italy
[2] SYSBIO-ISBE-IT-Candidate National Node of Italy for ISBE, Research Infrastructure for Systems Biology Europe, Milan, Italy
[3] Department of Chemical Science and Technology, University of Rome "Tor Vergata", Via della Ricerca Scientifica 1, 00133 Rome, Italy
[4] Institute of Molecular Bioimaging and Physiology, National Research Council, Via Fratelli Cervi, 93, 20054 Segrate (MI), Italy
[5] Department of Medicine and Surgery, University of Milano-Bicocca, Via Cadore, 48, 20900 Monza (MB), Italy
[6] Sbarro Institute for Cancer Research and Molecular Medicine, Center for Biotechnology, Department of Biology, College of Science and Technology, Temple University, 1900 North 12th Street Philadelphia, PA 19122, USA
[7] Department of Medical Biotechnologies, University of Siena, Viale Mario Bracci 16, 53100 Siena, Italy
[8] Vita-Salute San Raffaele University, Via Olgettina 58, 20132 Milan, Italy
[9] Department of Experimental and Clinical Medicine, University of Florence, Viale Morgagni 63, 50134 Florence, Italy
[10] Urological Research Institute, Division of Experimental Oncology, IRCCS San Raffaele Hospital, Via Olgettina, 60, 20132 Milan, Italy
[11] Institute of Bioimaging and Complex Biological Systems, National Research Council, Via Fratelli Cervi, 93, 20054 Segrate (MI), Italy.
† These authors equally contributed to this work
‡ Co-seniorship

giacomo.ducci@unimib.it (G.D.); ciufolini@scienze.uniroma2.it (G.C.); gloria.campioni@unimib.it (Gl.C.); valentina.pasquale@unimib.it (V.P.); giulia.gigliotti@unimib.it (G.G.); s.ponzetto@campus.unimib.it (S.P.); d.benedetti5@campus.unimib.it (D.B); brunogiovanni.galuzzi@cnr.it (BG.G.); deborah.daliberti@unimib.it (D.D.); s.spinelli22@campus.unimib.it (S.S.); vrundaben.satasiya@temple.edu (V.S.); ventura.elisa@hsr.it (E.V); chiara.raggi@unifi.it (C.R.); vago.riccardo@hsr.com (R.V.); marcella.bonanomi@cnr.it (M.B.); daniela.gaglio@cnr.it

(D.G.); antonio.giordano@temple.edu (A.G.); andrea.morrione@temple.edu (A.M.); chiara.damiani@unimib.it (C.D.); rocco.piazza@unimib.it (R.P.); cicero@scienze.uniroma2.it (DO.C.); marco.vanoni@unimib.it (M.V.); petrella@scienze.uniroma2.it (G.P.); elena.sacco@unimib.it (E.S.)

Correspondence: * elena.sacco@unimib.it (E.S.); ** petrella@scienze.uniroma2.it (G.P.); *** marco.vanoni@unimib.it (M.V.)

Abstract

Bladder cancer is one of the most common malignancies worldwide, impacting public health systems due to its high rate of recurrence. Metabolic alterations enable the identification of novel, needed prognostic markers and therapeutic vulnerabilities for precision oncology. Here, we use a systems metabolomic approach that integrates metabolic functional data with multi-omics, transcriptomics and metabolomics, through biostatistics and mathematical modelling to characterise metabolic rearrangements associated with *FGFR3* oncogenic activation, one of the most frequent lesions in bladder cancer. The analyses conducted on a panel of five human bladder cancer cell lines reveal a significant correlation between *FGFR3* alterations and the acquisition of a predominantly oxidative, poorly migratory phenotype, regardless of tumour progression. These preclinical results, validated through FGFR3 and oxidative phosphorylation pharmacological inhibition, and computational analysis on bladder cancer cell line and patient publicly available datasets, support the therapeutic potential of targeting oxidative metabolism in *FGFR3*-altered tumours, including more aggressive subtypes.

Keywords: systems biology; multi-omics data integration; bladder cancer cell lines; patient sample dataset; energy and redox metabolism; Seahorse Extracellular Flux Analyzer; NMR-based

exometabolomics; transcriptomics; mathematical modelling; oxidative phosphorylation; glycolysis

Introduction

Bladder cancer (BC) is the ninth most common cancer diagnosed worldwide. Global Cancer statistics (GLOBOCAN2022) revealed an incidence of approximately 614,000 new BC cases (3.0% of all cancer types) and 220,000 deaths (2.3% of all cancer-related deaths) occurring in 2022[1]. BC is more common in men, ranking sixth for incidence and ninth for cause of cancer death. Urothelial Bladder Carcinomas (UBC), also known as Transitional Cell Carcinomas, account for 90% of all BC diagnosed cases[2]. These cancers typically originate in the urothelial layer and may progress as the stages advance, directly invading the subepithelial connective tissue (submucosa/lamina propria), muscular layers, and serosa. These cancers can spread directly to nearby pelvic structures, such as prostate, urethra, vagina, uterus, and bowel. Lymphatic spread can occur through lymph nodes in the obturator, presacral, iliac, and para-aortic regions[3]. About 75% of UBC patients, classified as non-muscle-invasive bladder cancer (NMIBC), experience a condition where the disease is limited to the mucosa (pTa, Tis) or lamina propria (pT1). The remaining 25% of newly diagnosed urothelial bladder tumours, classified as muscle-invasive bladder cancer (MIBC), invade the bladder's muscle wall (pT2-pT4), a condition associated with significantly reduced life expectancy. Currently, the only molecular marker contributing to the stratification of BC patients, crucial for directing them to targeted treatments, is the presence of gain-of-function alterations of the tyrosine kinase receptors *FGFR* (Fibroblast Growth Factor Receptor), particularly *FGFR3*[4,5]. *FGFR3* alterations are associated with more than 60% of NMIBCs

and at least 15% of MIBCs[6,7]. The most common oncogenic mutations include S249C, R248C, and Y373C, which lead to constitutive activation of FGFR3 signaling, essential for various cellular processes, such as cell proliferation, migration, and survival, thereby promoting tumour growth. In addition to mutations or overexpression, FGFR3 is also activated in BC through chromosomal rearrangements that generate constitutively activated fusion genes, such as *FGFR3*-transforming acid coiled-coil 3 (*TACC3*) fusions resulting from 4p16.3 rearrangements[8]. Currently, the pan-FGFR inhibitor Erdafitinib is approved for the treatment of adults with locally advanced or metastatic urothelial carcinoma harbouring *FGFR2* or *FGFR3* alterations who have progressed following chemotherapy[9]. While an objective response rate of 40% has been reported, the complete response rate remains low at only 3%, with a median duration of response of 5.6 months[10–12]. Moreover, clinical trial data indicate that bladder cancer patients with FGFR fusions exhibit a lower response rate to Erdafitinib than those with *FGFR3* activating mutations (16% vs. 49%)[13]. These findings highlight that there is still a strong need for new therapeutic options for patients with FGFR alterations, especially in light of the potential intrinsic[14] and acquired resistance, the latter commonly observed following treatment with tyrosine kinase inhibitors. Ongoing research efforts are focused on developing more selective agents and evaluating synergistic pharmacological combinations[15–18], including those involving immunotherapy, as reviewed by Ascione et al., 2023[19].

Metabolic reprogramming is a recognized hallmark of cancer[20], including bladder cancer[21]. Among the most well-known metabolic alterations in cancer cells are aerobic glycolysis (the Warburg effect)[22–24], upregulation of the pentose phosphate pathway[25], the anaplerotic use of glutamine[26], changes in fatty acid and cholesterol metabolism[27], and disrupted reactive oxygen

species (ROS) homeostasis[28]. These alterations fulfil the increased demand for energy, building blocks, reducing power, and signaling molecules required to support rapid growth and ensure survival under conditions where normal cells do not proliferate or die, such as oxygen and nutrient limitations and oxidative stress[29]. The primary drivers of these metabolic rearrangements are the activation of specific oncogenes (including *RAS*, *EGFR*, *BRAF*, *cMYC*, and *HIF*) and the loss of specific tumour suppressors (including *TP53*), which influence gene expression of metabolic enzymes or key regulators of metabolism, such as PI3K and AMPK[30–33]. These metabolic changes, in turn, impact the cellular transcriptional program by fostering the acquisition of traits that contribute to tumour progression, including the epithelial-mesenchymal transition (EMT) and stemness involved in cell invasion, metastasis, and chemoresistance[34]. Thus, the characterization of metabolic alterations supporting tumour maintenance and progression may allow the identification of novel prognostic factors and/or therapeutic vulnerabilities[35–37].

In this work, we characterized morpho-functional features (proliferation rate, apoptosis, redox homeostasis, and migration) and metabolic behaviour (measuring extracellular metabolic fluxes using NMR and Seahorse technology) of a panel of five human UBC cell lines at various stages and grades of tumour progression. Integrating transcriptomic and exometabolomic data through a mathematical model of metabolism enabled the prediction of metabolic fluxes in the cell lines. In addition to highlighting the metabolic heterogeneity of the UBC cell lines, this analysis revealed a notable correlation between oncogenic activation of *FGFR3* and the acquisition of a predominantly metabolic oxidative, poorly migratory phenotype, exploitable from the perspective of metabolic-oriented therapies.

Results

Alterations in *FGFR3* impair cell lateral migration but do not correlate with other functional properties

To identify morphological and functional features associated with *FGFR3* gene alterations, we assembled a panel of five human UBC cell lines representative of different stages and grades of tumour progression, including both wild-type and *FGFR3*-altered cell lines. A NMIBC low-grade cell line RT112 carries a *FGFR3*-transforming acid coiled-coil 3 (*TACC3*) fusion. Four MIBC cell lines include the low-grade 5637 cell line (*FGFR3*-wt gene), and three high-grade cell lines: two with a wild-type *FGFR3* gene (UMUC3 and HT1376) and one carrying the gain-of-function *FGFR3*^{K652E} mutation (J82). ***Figure 1a*** and ***Supplementary Table 1*** summarize the main features of the five cell lines.

We first analysed properties related to tumour progression, including proliferation rate, oxidative stress, apoptosis, and migration.

Growth kinetics (***Supplementary Fig. 1a***) highlighted that the proliferation rate of the five UBC cell lines does not correlate with *FGFR3* alteration. In fact, all the cell lines of the panel have similar proliferation rates except for HT1376 and J82 cells, which show a significantly lower growth rate (***Fig. 1b***). Note that cell size measured as protein content (***Supplementary Fig. 1b***) and cell volume (***Supplementary Fig. 1c***), and chromosome number/degree of aneuploidy (***Supplementary Table 1***), varied significantly among cell lines with similar cell proliferation rates. For example, the smallest cells in the panel, 5637 (G2 pT2), proliferate just as fast as RT112 (G2 pT<2) and UMUC3 (G3 pT>2), which have approximately double protein content and different

aneuploidy degrees. This evidence demonstrates that, in addition to cell size, other factors contribute to controlling the proliferation rate of bladder cancer cell lines of our panel, which likely include signaling pathways and metabolic exchange rates, routes, and turnover[38].

To assess the impact of *FGFR3* alteration on redox homeostasis in UBC cell lines, we quantified glutathione by enzymatic assay (***Fig. 1c, d and Supplementary Fig. 1d, e***) and cytoplasmic ROS by quantitative imaging on DCFDA-stained cells (representative images and graph in ***Fig. 1e, f***). This analysis showed that NMIBC cell line RT112 has higher GSH levels and lower ROS levels than the MIBC cells (5637, UMUC3, HT1376, and J82), which correlated with reduced apoptosis measured as positivity to the fluorescent probe CellEvent (representative images and graph in ***Fig. 1g, h***). Note that none of these parameters regarding redox homeostasis correlate with the presence of *FGFR3* alterations.

Finally, wound healing experiments highlighted that a low lateral migration rate correlates with the presence of *FGFR3* alterations. In fact, among the four MIBC cell lines, only J82 carrying an altered *FGFR3,* showed low migratory capacity similar to the *FGFR3*-altered NMIBC cell line RT112 (***Fig. 1i, j***). However, lateral migration does not correlate with transwell migration capacity (***Fig. 1k, l***). Indeed J82 cell line is the most efficient in transwell migration, indicating that lateral and transwell migration are different properties. These data are consistent with literature findings (Liu et al. 2021; Pang et al. 2019). Notably, we previously demonstrated that the five UBC cell lines were separated based on staging for the presence of tunneling nanotubes (TNTs), open membranous channels which are involved in the transport of several cellular components and organelles, such as mitochondria[39]. Specifically, only cultures from the four MIBC cell lines,

independently from the presence of *FGFR3* alteration, were characterized by these functional nanostructures interconnecting the cells.

Alterations in *FGFR3* correlate with a predominantly oxidative phenotype

After analysing the morpho-functional properties of the UBC cell panel, we focused on the characterization of the metabolic features potentially affected by *FGFR3* alterations.

First, we analysed cellular bioenergetic parameters using Seahorse technology, which allows real-time measurements of oxygen consumption and extracellular acidification rates that account for mitochondrial and glycolytic activities respectively in live cells. The analyses were performed using a pharmacological perturbation protocol, which allows the calculation of basal, maximal, and spare (residual) mitochondrial respiratory (***Fig. 2a-c***) and glycolytic (***Fig. 2d-f***) capacity, normalized on cell number, as described in the *Materials and methods* section. We calculated the relative use of oxidative and glycolytic metabolism, which defines the predominant energy phenotype, as the ratio between basal mitochondrial respiration and basal glycolysis, as shown in ***Fig. 2g***. Note that this parameter is independent of the normalization method.

Seahorse analysis showed that the NMIBC cell line RT112 has a mainly oxidative metabolism (high basal and maximal mitochondrial respiration, low basal and maximal glycolysis ***Fig. 2a-g***), while MIBC cell lines showed a more heterogeneous metabolism. Specifically, 5637 and UMUC3 cells showed the lowest basal and maximal mitochondrial capacity (***Fig. 2a, b)*** and predominantly used glycolytic metabolism (***Fig. 2g).*** Instead, HT1376 and J82 can rely on both efficient mitochondrial and glycolytic machinery (high maximal respiration and maximal glycolysis, ***Fig. 2b, e***). However, while J82 cells in basal conditions made little use of glycolysis, displaying a predominantly

oxidative metabolic phenotype like RT112 (high basal respiration, low basal glycolysis ***Fig. 2a, d*** and ***g***), HT1376 cells showed both high basal respiration and glycolysis (***Fig. 2a, d***), resulting in the most energetic cell line of the panel. A low basal glycolytic flux in *FGFR3*-altered UBC cell lines (RT112 and J82) and HT1376 was observed using the CMV-Hylight Biosensor, a fluorescent biosensor for fructose 1,6-bisphosphate (FBP)[40] (***Fig. 2j*** and representative images in ***Supplementary Fig. 2d***). Note that this parameter is not normalized per cell and it is in line with the Seahorse basal glycolysis parameter normalized on protein content (***Supplementary Fig. 2e, f***).

Metabolic differences were also assessed in terms of ATP production through mitochondrial respiration or glycolysis, with RT112 and J82 cells, both carrying *FGFR3* alterations, endowed with an ATP production rate index (glycoATP/mitoATP), independent from the normalization method, lower of all other cell lines, due to low levels of ATP produced through glycolysis and high levels of ATP produced through mitochondrial respiration ***(Fig. 2h*** and ***Supplementary Fig. 2a-c***).

In conclusion, the five UBC cell lines under study can be divided into two energy metabolic groups: a predominantly oxidative group consisting of *FGFR3*-altered RT112 and J82 cell lines (group I), and a more heterogeneous but predominantly glycolytic group consisting of *FGFR3*-wt 5637 and UMUC3 cell lines (group II) (***Fig. 2g***). Based on the ratio between basal respiration and basal glycolysis reported in ***Fig. 2g***, *FGF3R*-wt HT1376 cells maintained a predominantly glycolytic phenotype (typical of group II), even if the behaviour is borderline. It is interesting to note that the prevailing glycolytic phenotype correlates with lower spare respiratory capacity, which is the amount of residual mitochondrial respiration not used in basal conditions but available to respond to sudden energy needs (***Fig. 2c***). Unsupervised hierarchical clustering of the five UBC

cell lines, performed considering all the Seahorse data, demonstrated a clear separation of cell lines according to the FGFR3-activation state (***Fig. 2i***).

We then analysed metabolites present in the culture medium at 0 and 48 hours of growth using ^{1}H-NMR. We identified and quantified 39 metabolites, 14 of which were consistently consumed, 8 were consistently excreted, and 17 were variably consumed or excreted depending on cell line (***Supplementary Table 2***). Firstly, we explored the metabolic correlations among all exometabolomic variables through an unsupervised hierarchical clustering model, shown in the heatmap in ***Figure 2k***. We decided to include in the analysis four metabolic ratios reflecting distinct metabolic behaviours: (i) lactate/glucose, which underscores the extent of the Warburg effect, namely the reliance on glycolysis for energy production even in normoxic condition[41], significantly higher in MIBC cell lines (***Supplementary Fig. 3a***); (ii) lactate/alanine, indicative of the oxidative status of the cell, reflecting the interplay between glycolysis and pyruvate transamination, with lower ratios suggesting increased alanine production and a more reduced intracellular environment[42], significantly lower in *FGFR3*-altered cell lines RT112 and J82 (***Supplementary Fig. 3b***); (iii) glutamate/glutamine, which measures a cell's relative capacity of glutaminolysis and actual intracellular usage of glutamate[43], significantly higher in high grade cell lines (***Supplementary Fig. 3c***); (iv) glutamate/cystine, highlighting the role of glutamate in cystine uptake, which is critical for glutathione synthesis and oxidative stress defense[44], significantly higher in high grade cell lines (***Supplementary Fig. 3d***).

Unlike Seahorse data, exometabolomic variables showed a more complex clustering that did not group samples based on the presence of *FGFR3* alteration, nor by BC progression (staging or grading). However, taking a closer look at metabolites involved in energy metabolism, a strong correlation between metabolite exchange rates and Seahorse parameters was observed (***Fig. 2l-n***, ***Supplementary Fig. 3e***), also according to the basal glycolytic flux measured using CMV-Hylight Biosensor (***Supplementary Fig. 3f***). Particularly, glucose consumption and lactate excretion correlated with glycolytic but not respiratory levels, while glutamine consumption paired with respiratory levels, suggesting a specific use of nutrients for energetic demand.

Starting from these correlations, we combined exometabolomics and Seahorse data using an unsupervised hierarchical clustering model illustrated in the heatmap in ***Figure 3a***. We applied Unit-Variation scaling to the absolute values of the exchange rates to ensure that all features contribute equally to the model, regardless of whether the metabolites were consumed or excreted.

This analysis revealed structured relationships between Seahorse parameters and NMR-based exometabolomics data. Specifically, two key clusters (C7 and C11) comprised Basal Respiration, Maximal Respiration, Spare Respiratory Capacity, and mitochondrial ATP production, closely associated with glutamine consumption and glutamate excretion. This grouping suggested a link between intracellular ATP generation related to mitochondrial respiration and glutaminolysis, one of the main energy routes to fuel TCA cycle and oxidative phosphorylation. Another cluster (C2) grouped glycolytic ATP production and Basal Glycolysis with glucose consumption and lactate excretion, reinforcing a connection between glycolytic flux and extracellular glucose and lactate turnover.

Notably, the hierarchical clustering of UBC cell lines based on their metabolic profiles divided them into two main groups: one consisting of RT112, and J82 (harbouring *FGFR3* alterations), along with HT1367 (*FGFR3* wild-type); the other including 5637 and UMUC3, both *FGFR3* wild-type. Interestingly, although the HT1376 was grouped with the *FGFR3*-altered cell lines, it exhibited a heterogeneous metabolic phenotype. Indeed in C2 cluster, including glycolytic pathway parameters they more closely resemble UMUC3 cells, which carry wild-type FGFR3 (***Fig. 3a***).

We then combined exometabolomics and Seahorse data using a supervised multivariate model analysis based on the presence or absence of *FGFR3* alteration. The OPLS-DA model (***Fig. 3b, c***) was calculated using the same variables considered in the unsupervised clustering shown in ***Fig. 3a***, scaled by Unit-Variation. This analysis revealed a clear metabolic distinction between *FGFR3*-altered and wild-type *FGFR3* UBC cell lines (***Fig. 3b***). Despite J82 cells derive from an aggressive tumour model, unlike RT112, the OPLS-DA separating *FGFR3*-altered from *FGFR3*-wt cells remains statistically robust, demonstrating that the correlation between metabolic phenotype and *FGFR3* alteration highlighted in ***Fig. 2i*** is highly significant, regardless of grade and stage. Metabolites and metabolic features mostly contributing to the classification are those with Variable Importance in the Projection (VIP) > 1 and highlighted in red in the loading plot (***Fig. 3c***). *FGFR3*-wt cells were characterized by high glucose consumption, lactate excretion, ATP index and lactate-to-glucose ratio, supporting a glycolysis-driven metabolic phenotype. In contrast, *FGFR3*-altered cells exhibited high reliance on mitochondrial metabolism, with key contributors including fumarate and citrate, indicative of enhanced TCA cycle activity. *FGFR3*-altered cells also displayed high glutamine and glycine consumption, reinforcing the role of amino acid catabolism

in sustaining oxidative phosphorylation. Increased mitochondrial ATP production, basal respiration, and maximal respiration further confirmed an acquired shift toward oxidative phosphorylation in *FGFR3*-altered cells. Interestingly, *FGFR3*-altered cells preferentially consume glycine, whereas *FGFR3*-wt cells predominantly excrete it. Glycine plays a central role in one-carbon metabolism, serving as a key precursor for nucleotide biosynthesis, methylation reactions, and redox balance[45,46]. The differential handling of glycine between these two groups suggests distinct metabolic demands.

These findings suggest that the heterogeneity observed in exometabolomics, encompassing various metabolites involved in distinct biological functions, may cover differences specifically related to energy metabolism. Interestingly, integrating these data with Seahorse analysis allowed for clearer interpretation, leading to more reliable results.

To explore the intracellular metabolism of the UBC cell lines, complementary to metabolic fluxes, we performed endometabolomic analysis by LC-MS. Endo-metabolomic analysis identified 152 metabolites. Metabolic correlations among all endometabolomic variables was explored through an unsupervised hierarchical clustering model, shown in the heatmap in Figure 4a.

Unsupervised clustering showed that the five cell lines are grouped by *FGFR3* allelic status, consistent with the results reported in ***Fig. 3a*** (exo-metabolome/Seahorse data integration). Metabolite enrichment analysis with the MetaboAnalyst software suite indicated that different pathways involved in energetic metabolism are differentially expressed between the *FGFR3*-wt and the *FGFR3*-altered groups (***Fig. 4b***). These pathways include the citric acid cycle, glutamate metabolism, the glucose-alanine cycle, and the mitochondrial electron transport chain (black

arrows in Fig. 4b), and are consistent with the metabolic fluxes determined by the Seahorse technology.

Analysis of endo-metabolomic data showed in *FGFR3*-altered cell lines (i) reduced intracellular levels of glutamine (***Fig. 4a***, green arrow), along with an increased intracellular glutamate/glutamine ratio more pronounced in the J82 cell line (***Fig. 4c, Supplementary Fig. 3j***); (ii) reduced NADH levels (Fig. 4a, red arrow) indicating higher mitochondrial oxidative metabolism, in keeping with the Seahorse data; (iii) reduced intracellular lactate/alanine ratio (***Fig. 4d, Supplementary Figure 3h***), indicating that pyruvate fluxes are more strongly directed toward alanine than to lactic fermentation (lactate/glucose ratio in ***Supplementary Fig. 3g***), with the decreased ratio mainly due to increased alanine levels (***Fig. 4a***, purple arrow).

Transcriptomic analyses confirm *FGFR3*-altered UBC cells' shift toward oxidative metabolism

To get further insight into the functional role of *FGFR3* alteration in the five UBC cell lines, we performed transcriptomics analysis, focusing on genes differentially expressed between the *FGFR3*-wt and *FGFR3*-altered groups. Gene Set Enrichment Analysis (GSEA) using the Hallmarks gene sets (50 gene sets summarizing and representing specific well-defined biological states or processes and displaying coherent expression) (***Fig. 5a***) showed a downregulation of genes involved in the epithelial-mesenchymal transition in the *FGFR3*-altered group, in line with the results of the wound healing assay shown in ***Figure 1j***. Other gene sets downregulated in this group referred to cell proliferation (i.e. KRAS signaling, mitotic spindle). Moreover, the *FGFR3*-altered group showed an upregulation of the interferon pathways and in several gene sets

involved in lipid metabolism (i.e. mTORC1 signaling, adipogenesis, cholesterol homeostasis, and fatty acid metabolism) and redox homeostasis, suggesting the role of FGFR3 in these pathways. Notably, one of the most significant upregulated gene sets in the *FGFR3*-altered group was oxidative phosphorylation (***Fig. 5a***), in line with the predominantly oxidative phenotype observed with the metabolic analysis previously described.

To further focus on the different metabolic rearrangements characterizing *FGFR3*-wt and *FGFR3*-altered groups, we used a computational pipeline that integrates exometabolomics and transcriptomics data, i.e. the INTEGRATE model, based on the ENGRO2 core model as a metabolic network[47,48], selecting constraint-based stoichiometric metabolic models as a scaffold. Transcript levels were converted into Reaction Activity Scores (RASs), namely enzymatic activities according to the expression of their associated genes and the relationship among them encoded within GPR (Gene-Protein-Reaction) associations[49]. We selected exchange rates of 19 metabolites from exometabolomics (i.e. alanine, aspartate, cystine, glucose, glutamate, glutamine, glycine, histidine, isoleucine, lactate, leucine, lysine, methionine, phenylalanine, pyruvate, serine, threonine, tyrosine, valine) as constraints for the model, in terms of consumed and excreted metabolites to fuel cell metabolism, and used the upper and lower values of exchange rates as upper and lower bounds of the corresponding exchange reactions. We then reported the predicted fluxes on a map showing the main reactions of central carbon metabolism (***Fig. 5b***), grouping cell lines for the presence of *FGFR3* alterations. The analysis revealed that the *FGFR3*-altered group presents upregulation of the second, third, and fourth complexes of the electron transport chain, along with a higher activity of the TCA cycle, fueled by glutaminolysis, and the fatty acids β-oxidation, suggesting a high reliance on mitochondrial activity in these cells. On the

contrary, we observed an upregulation of the whole glycolytic pathway and lactic acid fermentation in the *FGFR3*-wt group.

To verify the translatability in bladder tumours of the metabolic features observed in our cell panel, we extended the computational analysis to publicly available larger bladder cancer sample datasets, such as (i) the CCLE dataset, which contains bulk transcriptomic data from 17 human bladder cancer cell lines (11 FGFR3-wt lines and 6 FGFR3-altered lines), including all 5 cell lines of our UBC panel, and (ii) the TCGA dataset of muscle-invasive bladder cancer samples from 408 patients (TCGA, Cell 2017[50]). Firstly, we performed GSEA analysis using the Hallmarks gene sets previously applied to the transcriptomes of the cells of our UBC panel. Analysis confirmed in CCLE bladder cancer cell lines (***Supplementary Fig. 4a***) and in MIBC patient samples (***Fig. 6a***) a dysregulation in line with the one observed in our UBC panel. Specifically, oxidative phosphorylation was upregulated in the *FGFR3*-altered group, together with adipogenesis. Moreover, epithelial to mesenchymal transition was one of the most significantly downregulated gene sets in the *FGFR3*-altered group, followed by several gene sets related to proliferation and immune response. Since public datasets containing both transcriptomic and exometabolomic data from patient samples are unavailable, we could not perform the INTEGRATE-based computational analysis applied to UBC cell lines reported in ***Fig. 5b***, and proceeded only to map RASs derived from the transcriptomic data on the ENGRO2 model, grouping BC samples, cell lines (***Supplementary Fig. 4b***) and patients (***Fig. 6b***) by the presence of alterations in *FGFR3*. We analogously processed transcriptomic data from our cell panel (***Supplementary Fig. 5***) for a direct comparison. The analysis revealed in both patient samples and our cell models an upregulation of complexes of the electron transport chain in the *FGFR3*-altered group, along with a

downregulation of glucose fermentation bottleneck reactions i.e. glucose intake, glucose phosphorylation to glucose-6-phosphate and lactate production from pyruvate, supporting the energetic shift toward oxidative metabolism in bladder cancer cells carrying altered *FGFR3*.

FGFR3 and OXPHOS pharmacological inhibition in UBC cell lines

To validate the correlations between FGFR3 alterations and OXPHOS enhancement, previously identified through functional, omics, and computational analyses, we evaluated the impact of FGFR3 inhibition on UBC cell lines. Specifically, we assessed cell proliferation and viability/mortality via growth kinetics, alongside mitochondrial bioenergetics using Seahorse XF technology, in cells treated with increasing concentrations of Erdafitinib, a pan-FGFR inhibitor approved for the treatment of adults with locally advanced or metastatic urothelial carcinoma harbouring *FGFR3* alterations. Consistent with our findings, Erdafitinib exerted dose-dependent antiproliferative and cytotoxic effects selectively on the *FGFR3*-altered RT112 and J82 cell lines (***Fig. 7a, b*** and ***Supplementary Fig. 6a-j***), with the latter showing lower sensitivity according to the literature[51]. Seahorse XF analyses, performed on cells treated with Erdafitinib for 24 hours (the time at which no effect on cell viability was observed), showed a significant reduction in both basal and maximal mitochondrial respiration in these two cell lines, supporting the hypothesis that *FGFR3* gene alteration drives increased mitochondrial respiration (***Fig. 7c, d***). Notably, a significant reduction of ATP produced via mitochondrial respiration was observed only in Erdafitinib-treated RT112 cells (***Fig. 7e***).

We further investigated the effects of pharmacological inhibition of mitochondrial respiration using IACS-010759, a clinical-stage Complex I inhibitor. Treatment induced a dose-dependent antiproliferative effect across all tested cell lines (***Fig. 7f*** and ***Supplementary Fig. 6k-o***). However,

cytotoxic effects were limited to RT112, J82, and HT1376 cells, suggesting a greater dependency on oxidative metabolism in these specific cell lines (***Fig. 7g*** and ***Supplementary Fig. 6p-t***). Notably, previous Seahorse analysis confirmed that HT1376 possesses a more efficient respiratory machinery compared to other FGFR3 wild-type cell lines. Consistent with our hypothesis, OXPHOS inhibition significantly reduced cell viability in the most respiratory cell lines, including the *FGFR3*-altered RT112 and J82. Collectively, these findings suggest that targeting oxidative metabolism may represent a promising therapeutic strategy for *FGFR3*-altered bladder cancer.

Discussion

FGFR3 oncogenic activation represents one of the most common genetic alterations in bladder cancer, particularly prevalent in non-muscle invasive tumours (over 60%) and also detected in more than 15% of high-grade, muscle-invasive bladder cancers[52,53]. Targeted therapies against FGFR have been developed and are currently approved only for chemotherapy-resistant MIBC patients[5]: their limited efficacy, likely due to low selectivity and both intrinsic and acquired resistance mechanisms[54], highlights the need for continued efforts by the scientific community to identify more effective treatment options.

This paper investigates metabolic rewiring associated with *FGFR3* alterations to identify metabolic features or vulnerabilities that could be exploited in future precision oncology interventions. Indeed, changes in metabolic states not only sustain the enhanced growth and survival of cancer cells[29] but also underlie physiological changes that drive tumour progression[55]—such as the enhancement of migratory capabilities, epithelial-to-mesenchymal

transition[56,57], stemness[58], and the ability to shape the tumour microenvironment[59]—and influence the response to pharmacological treatments, including chemotherapy resistance[60,61]. Therefore, targeting metabolic states can affect and rewire all the above-reported physiological alterations that contribute to tumour progression and can improve patient outcomes.

A schematic workflow of the study is presented in ***Graphical Abstract***. Specifically, we analyzed the metabolic profiles of five human urothelial bladder cancer cell lines at different stages and grades using an unbiased, top-down systems metabolomics approach that integrates functional metabolic data and transcriptomics through mathematical modelling[62]. The panel includes cell lines with *FGFR3* alterations derived from both non-muscle-invasive (RT112) and muscle-invasive (J82) bladder cancers.

Integrating Seahorse metabolic flux analysis with NMR-based exometabolomics revealed two distinct metabolic groups among the five UBC cell lines, reflecting their *FGFR3* alteration status, regardless of tumor grade and stage. This is the first time that Seahorse-derived metabolic parameters have been systematically linked to NMR-based exometabolomics data, offering new insights into the relationship between energy metabolism and metabolite exchange dynamics. The same clustering was achieved using 152 intracellular metabolites identified by LC-MS. Transcriptomic and exo-metabolomic data were employed to constrain a mathematical model of metabolism. Overall, the analyses showed that *FGFR3*-altered cells exhibited an oxidative metabolic profile, marked by increased glutaminolysis and fatty acid β-oxidation to support the TCA cycle and mitochondrial ATP production for both biosynthesis and energy needs confirming the well-established role of glutaminolysis in fuelling oxidative phosphorylation (OXPHOS) in mitochondrial-dependent cancer cells[63,64]. Additionally, *FGFR3*-altered cells actively consume

glycine, a crucial precursor for TCA cycle intermediates and glutathione synthesis, indicating its role in anaplerosis and oxidative stress defense, typical of tumors dependent on oxidative phosphorylation[65]. In contrast, *FGFR3*-wt cells displayed a glycolytic phenotype with high glucose consumption dedicated to lactate fermentation for ATP generation, and elevated excretion of formate, glycine, and myo-inositol, pointing to an upregulated one-carbon metabolism essential for nucleotide synthesis and amino acid turnover, characteristic of tumors exhibiting the Warburg effect[45,46]. Notably, *FGFR3*-wt cells also had low spare respiratory capacity, i.e., the residual OXPHOS not used under basal conditions but available to meet sudden energy demands. Low spare respiratory capacity may indicate mitochondrial exhaustion even when basal mitochondrial respiration appears normal[66], justifying the common reliance on glycolysis. Conversely, *FGFR3* alterations appear to enhance mitochondrial plasticity by increasing spare respiratory capacity. While a higher spare capacity often implies metabolic resilience, this shift also reflects a profound rewiring toward an active oxidative phenotype. This increased engagement of mitochondrial respiration in *FGFR3*-altered cells may create a specific metabolic vulnerability, rendering them susceptible to mitochondrial inhibitors.

Here, we report pharmacological results that align with these observations.

The specific FGFR3 inhibitor erdafitinib exerts a dose-dependent cytotoxic and antiproliferative effect only in cells with an altered *FGFR3* gene (RT112 and J82, ***Fig. 7***). The lower sensitivity of the J82 cells aligns with existing literature, which suggests that these cells have some intrinsic resistance to FGFR3 pharmacological treatment[51]. This cytotoxic effect is accompanied by a reduction in both basal and maximal mitochondrial respiration. Furthermore, pharmacological inhibition of mitochondrial respiration with IACS-010759, currently in clinical trials, induces cell

death in the *FGFR3*-altered cell lines RT112 and J82. Only the HT1376 line, the more oxidative among the *FGFR3*-wt cell lines, shows cell death upon treatment with the inhibitor. These pharmacological findings indicate that (i) the *FGFR3* gene alteration drives increased mitochondrial respiration, and (ii) targeting oxidative metabolism may be a viable strategy for treating *FGFR3*-altered bladder cancer.

To extend our observations to patient samples and strengthen their clinical relevance, we leveraged a publicly available transcriptomic dataset of bladder cancer samples stratified based on the presence of *FGFR3* alterations[50]. Transcriptomic analysis of both cell lines and patient samples further showed dysregulation of gene sets associated with cytokine production and immune response pathways in *FGFR3*-altered samples, in line with previously published data[67,68]. In this regard, Ouyang et al. reported that the immunosuppressive phenotype of *FGFR3*-altered tumour cells may be driven by enhanced serine synthesis efflux, resulting from upregulation of serine biosynthesis, particularly involving the reaction catalysed by the enzyme PSAT1. Although our mathematical model highlighted an upregulation of the PSAT1-catalyzed reaction, exometabolomics analysis did not detect a significant increase in serine efflux in *FGFR3*-altered UBC cell lines. These discrepancies may be due to differences in experimental design: while Ouyang's study utilized isogenic models—human T24 and murine MB49 cell lines engineered to express mutant FGFR3—we compared distinct cell lines with *FGFR3* alterations occurring under different genetic backgrounds. The analyses also revealed that the epithelial-to-mesenchymal transition (EMT) gene set is downregulated in *FGFR3*-altered samples. This finding is consistent with the low lateral migratory capacity observed in *FGFR3*-altered cell lines, even if it is not in line with the transwell migration. In fact, J82, which is the cell line that migrates the least laterally in

the wound healing assay, is the one that migrates the most in the transwell assay, and conversely, the cell line that is fastest at closing the wound, 5637, is the one that migrates the least in the transwell. These data, although peculiar, are in keeping with the literature[69,70], demonstrating that the two types of migration in bladder cancer depend on different properties.

Then, we mapped onto the mathematical model of the central carbon metabolism ENGRO2 the differential level of metabolic reaction activities of both the *FGFR3*-altered bladder cancer cell lines and patient samples, compared to their *FGFR3* wild-type counterparts. Despite the inherent heterogeneity of clinical samples, including contributions from stromal and immune compartments, transcriptome-constrained metabolic modeling recreated the metabolic phenotype observed in vitro. Notably, *FGFR3*-altered tumors display increased electron transport chain activity alongside decreased glycolytic reliance, highlighting a shift toward oxidative phosphorylation.

In summary, our integrative multi-level analyses—covering transcriptomics, endo- and exo-metabolomics, and metabolic flux measurements—demonstrate a strong connection between *FGFR3* alterations and distinct metabolic and functional reprogramming in bladder cancer, regardless of tumor grade and stage. Notably, our results suggest that *FGFR3* alterations surpass traditional histopathological classification in defining the metabolic behavior of urothelial bladder cancer. Pharmacological targeting of FGFR3 signaling and mitochondrial respiration consistently showed a dependence on FGFR3-driven metabolic states, with inhibition causing allele-specific cytotoxic effects. This underscores the therapeutic potential of targeting oxidative phosphorylation in *FGFR3*-driven tumors, including aggressive and treatment-resistant subtypes, within a precision oncology framework.

More broadly, this study exemplifies the power of systems biology approaches that integrate multi-omics and functional data with quantitative modeling to reveal clinically actionable metabolic vulnerabilities.

Methods

Cell cultures

A panel of five human urothelial bladder cancer cell lines was assembled for this study to cover different grades (G) and stages (pT) of cancer progression: one NMIBC cell line RT112 (G2 pT<2; low-grade tumour with moderately differentiated cells, deep invasion of lamina propria), and four MIBC cell lines 5637 (G2 pT=2; low-grade tumour with moderately differentiated cells invading muscolaris propria), UMUC3 (G3 pT>2 high-grade tumour with poorly differentiated cells deeply invading muscolaris propria), HT1376 (G3 pT>2 high-grade tumour with poorly differentiated cells and deeply invading muscolaris propria) and J82 (G3 pT3 high-grade tumour with poorly differentiated cells and significant invasion of deeper layers).

RT112 and 5637 cell lines were purchased from American Type Culture Collection (ATCC, Manassas, VA, USA). UMUC3 and J82 cell lines were purchased from Elabscience (Houston, TX, USA), while HT1376 cell line was from Sigma-Aldrich.

All cell lines were routinely grown in RPMI-1640 medium (R0883-Merck Life Science, Darmstadt, Germany) supplemented with 10% fetal bovine serum (FBS, Gibco™-ThermoFisher, Waltham, MA, USA), 4 mM glutamine, 100 U/mL penicillin, and 100 mg/mL streptomycin, at 37 °C in a humidified atmosphere of 5% CO_2. Cells were passaged when they reached sub-confluence

(typically twice a week) using trypsin-ethylenediaminetetraacetic acid (EDTA). Cells were maintained in culture for no more than one month (8 passages) after thawing.

Assays on adherent cells were performed in experimental medium: DMEM w/o phenol red (A1443001-Gibco™-Thermo Fisher Scientific), FBS 10%, 10 mM glucose, 2 mM glutamine, 100 U/mL penicillin and 100 mg/mL streptomycin.

All the cell line cultures were periodically tested for mycoplasma contamination by MycoBlue Mycoplasma Detector kit (ref. D101-02, Vazyme). Moreover, cell lines were authenticated and the genetic characteristics were determined by PCR-single-locus-technology (Eurofins Genomics Europe).

Growth kinetics

Cell proliferation was analysed by growth kinetics: 2.1 x 10^4 cells were plated in Cell Imaging 24-well Plates (glass bottom 170 µm thick, Eppendorf) in 500 µL of maintenance medium and incubated at 37 °C and 5% CO_2 overnight. After 24 h medium was changed, and cells were transferred to experimental medium. After a medium change, cells were grown for 24, 48 and 72 hours and then stained with Hoechst 33342 (working concentration 1 ug/mL incubated for 15 min at 37 °C and 5% CO_2). Cell growth was monitored through imaging acquisitions using Operetta CLS™ high-content analysis system in brightfield and widefield fluorescence microscopy using 10x magnification, and total cell count (nuclei positive for Hoechst 33342) was obtained using the Harmony software.

Growth kinetics under drug treatment

Cell proliferation and mortality were tested in presence of Erdafitinib, an FGFR3 inhibitor (ref. T3726 Targetmol Chemicals Inc.), or IACS-010759, an ETC complex I inhibitor (ref. HY-112037A, MedChem Express), at increasing concentrations (0.5, 5, 50, 500 nM for both drugs). Cell number was monitored as explained above, staining cells with Hoechst 33342, at 24, 48 and 72h after medium change. To evaluate mortality, cells were stained using Propidium Iodide (PI, working concentration 5 µg/mL, incubated with Hoechst 33342 for 15 min at 37 °C and 5% CO_2). Cell mortality (%) was obtained as ratio between Hoechst- and PI-positive nuclei and Hoechst-positive nuclei using the Harmony software.

Cell volume and cell protein content

1.4 x 10^5 cells/well were plated onto 6-well plates in maintenance medium and incubated at 37 °C and 5% CO_2 overnight. The next day, medium was changed to experimental medium, and cells were grown for 2 days. Cells were then detached using trypsin-EDTA, and suspensions were filtered through 70 µm filters, centrifuged, and resuspended in PBS. Live cells were counted using trypan-blue exclusion technique, and percentage of dead cells was calculated. Cell volume was determined using Coulter counter-Z1 Dual Cell and Particle Counter (Beckman Coulter, Life Sciences, CA, United States). For sample analysis, 2 x 10^5 live cells were diluted in 10 mL of 0.9% NaCl solution, mixed and read at the instrument. Each sample was read in technical duplicate.

Determination of protein content was performed using Protein Assay Dye Reagent Concentrate (#500.0006, Bio-Rad, CA, United States). After cell count, 10^5 live cells were transferred to a centrifuge microtube and centrifuged. The supernatant was removed, and cell pellets were

stored at -80°C till the day of the assay. For Bradford assay, samples were thawed, resuspended in 100 µL of NaOH 1M and incubated for 30 minutes at RT. After the incubation, 100 µL of HCl 1M were added to samples pipetting several times to obtain a homogeneous solution. Bradford reagent was prepared, and samples and BSA (standard curve) were diluted following manufacturer's instructions. VICTOR X3^{TM} microplate reader (Perkin Elmer, MA, USA) was used to read absorbance of samples at 570 nm. Results were normalized for cell number, adjusting number of live taken cells with respective dead cells percentages.

Glutathione levels

1.4 x 10^5 cells/well were plated in 6 well plates in maintenance medium and incubated overnight at 37 °C and 5% CO_2. The next day, medium was changed to experimental medium, and cells were grown for 2 days. Cells were then detached using trypsin-EDTA, and suspensions were filtered through 70 µm filters, centrifuged, and resuspended in PBS. Live cells were counted using trypan-blue exclusion technique. 10^5 cells were then collected and processed following the manufacturer's instructions (Glutathione Fluorescent Detection Kit, cat. EIAGSHF, Invitrogen, CA, USA).

Redox Homeostasis (cytoplasmic ROS)

1.5 x 10^4 cells/well were plated onto CellCarrier-96 Ultra Microplates 96-well (PerkinElmer) in maintenance medium and incubated overnight at 37 °C and 5% CO_2. The next day, cells were washed once with 150 µL of PBS with calcium and magnesium and stained with 10 µM H_2DCFDA (20 mM stock in DMSO), incubating the plate for 10 minutes at 37 °C and 5% CO_2. Following imaging acquisition of the dye, cells were stained with Hoechst 33342 (1 µg/mL incubated for 15

min at 37 °C and 5% CO_2), and further imaging acquisitions were done using Operetta CLS™ with 40x magnification with widefield fluorescence set-up. Dye quantitative analysis and total cell count (nuclei positive for Hoechst 33342) were obtained using Harmony software, as previously reported[71].

Cell death (apoptosis)

8 x 10^3 cells/well were plated onto a 96 well plate in maintenance medium and incubated overnight at 37 °C and 5% CO_2. The next day, medium was changed to experimental medium, supplemented with 2 µM of CellEvent™ Caspase-3/7 Detection Reagent (C10427, Invitrogen™-Thermo Fisher Scientific), and cells were grown for 24 hours. After 24 hours, cells were stained with Hoechst 33342 (working concentration 1 µg/mL incubated for 15 min at 37 °C and 5% CO_2), and counted using Harmony software (nuclei positive for Hoechst 33342). Mean CellEvent™ intensity per cell was then calculated.

Lateral migration

Cell lateral migratory capacity was tested using a wound healing assay, i.e. capacity of cells to close a wound in a cell monolayer (or scratch). The assay was performed as follows:

Day -2: cells, previously plated at a density of subconfluence, were stained for 30 minutes at 37 °C with 5 µM CellTracker™ Red CMTPX Dye (C34552, stock 10 mM in DMSO, Invitrogen™-Thermo Fisher Scientific), preceded and followed by one wash with PBS with calcium and magnesium.

Day -1: cells were detached using trypsin-EDTA as usual and resuspended in experimental medium. Cells were counted using trypan-blue exclusion technique and plated at confluence

density ($2.5x10^5$ cells/well) in 24 well Cell Imaging Plate (glass bottom 170 µm thick, Eppendorf) in 300 µL of final volume.

Day 0: cells are treated with Mitomycin C, to inhibit proliferation, adding 300 µL/well of drug 2x and incubating for 2h at 37°C. Proper Mitomycin C concentration for each cell line was obtained from a previous dose-response assessment on the complete panel: for all cell lines a final concentration of 2.5 µM was used, except for J82 that were incubated with 1 µM final concentration of Mitomycin C. After the incubation, cells were washed once with PBS; the scratch was performed with a p10 tip, using a support as guide designed and 3D printed by our lab (contact authors for the 3D model), and cells were washed again. Then, a volume of 500 µL of experimental medium, supplemented with 2 µM of CellEvent™ Caspase-3/7 Detection Reagent (C10427, Invitrogen™-Thermo Fisher Scientific), was added to each well. Wound coverage was monitored with automatized time-lapse imaging acquisition using Operetta CLS™, acquiring every entire well of the 24-well plate, both in brightfield and widefield fluorescence microscopy, using 10x magnification, every ~30 min (time of acquisition of the entire plate) for 24 h with monitored temperature (37 °C) and atmosphere (5% CO_2). Migration speed and migration leading edge morphology were evaluated using the Harmony software.

Before and after the time-lapse, cell number was determined by staining nuclei with Hoechst 33342 1 µg/mL (H3570, stock 10 mg/mL in water, Invitrogen™-Thermo Fisher Scientific) and counting with Operetta CLS™ and Harmony software.

Transwell migration

Cell transwell migratory capacity was tested using transwell migration assay, i.e. capacity of cells to through a membrane insert (insert pores size: 8 µm, ref. 3464, Corning). The assay was performed as follows:

Day -1: 10^6 cells are plated in a p60 petri dish.

Day 0: cells are treated with Mitomycin C, to inhibit proliferation, changing medium and adding 4mL of drug and incubating for 2h at 37°C. Proper Mitomycin C concentration for each cell line was obtained from a previous dose-response assessment on the complete panel: for all cell lines a final concentration of 2.5 µM was used, except for J82 that were incubated with 1 µM final concentration of Mitomycin C. After the incubation, cells were detached using trypsin-EDTA as usual and resuspended in experimental medium 0% FBS. Cells were counted using trypan-blue exclusion technique and plated at concentration of 50 cells/insert in 300 uL of experimental medium 0% FBS. After 10 minutes of incubation at room temperature, 700 uL of experimental medium 1% FBS were added in the lower section.

Day 1: after 18h of transwell migration, cells on the upper side of the membrane were removed by scraping, and, after 2 washes in PBS, cells were fixed using PFA 4% (incubation 20 minutes at room temperature) by immersion in a new well with 800 uL of solution. After 2 washes in PBS, cell nuclei were stained using Hoechst 33342 1 µg/mL (H3570, stock 10 mg/mL in water, Invitrogen™-Thermo Fisher Scientific) and counting was performed with Operetta CLS™ and Harmony software. Meanwhile, cells migrated in the lower section and detached from the

membrane were counted by collecting the medium in the lower section and cell number was determined by trypan-blue exclusion technique.

Cellular bioenergetics

Seahorse assays were performed according to the manufacturer's instructions. Cells were seeded onto Seahorse XF plates at a density of 2 x 10^4 cells/well in maintenance medium and cultured for 24 h. The next day, the medium was replaced with Seahorse XF DMEM Medium, pH 7.4, supplemented with 10 mM D-Glucose, 2 mM L-Glutamine and 1 mM Na-Pyruvate and cell cultures were allowed to equilibrate for 1h at 37 °C in a no-CO_2 incubator.

At the end of the Seahorse measurements, Hoechst 33342 was added to each well at the final concentration of 1 µg/mL and, after 15 min incubation, nuclei/well were imaged and counted by Operetta CLS™ software Harmony and directly used to normalize the Seahorse parameters per cell number[72].

The sensor cartridge hydration and loading were performed according to manufacturer's instructions.

For the assays, following drugs, and respective concentrations, were used:

- Oligomycin: 1.5 µM
- FCCP: 0.5, 1, 1.5 µM: for the determination of maximal respiration parameter, the FCCP concentration for each cell line was chosen after a dose-response curve (lowest concentration with the highest response, see ***Supplementary Fig. 7a***). 0.5 µM was chosen

for RT112 and 5637 cell lines, while 1 µM was chosen for UMUC3, HT1376 and J82 cell lines.

- Rotenone/Antimycin A: 0.5 µM (both drugs)

Seahorse XF assays parameters calculation

Respiratory parameters:

$$Basal\ respiration\ (MitoOCR_{Basal}) = OCR_{Basal} - OCR_{Rot/AntA}$$

$$Maximal\ respiration = OCR_{FCCP} - OCR_{Rot/AntA}$$

$$Spare\ respiratory\ capacity = OCR_{FCCP} - OCR_{Basal}$$

$$ATP\text{-}linked\ respiration\ (OCR_{ATP}) = OCR_{Basal} - OCR_{Oligomycin}$$

Where:

OCR_{Basal} *= last OCR measurement before the first injection*

OCR_{FCCP} *= highest OCR value after FCCP injection*

$OCR_{Rot/AntA}$ *and* $OCR_{Oligomycin}$ *= lowest OCR values after Rot/AntimycinA and oligomycin injections respectively*

The determination of glycolytic and ATP production parameters was derived from formulas presented by Mookerjee *et al.*[73,74].

Glycolytic parameters:

$$Basal\ glycolysis = PPR_{Glyco} \times BP$$

$$Maximal\ glycolysis = [(ECAR_{Rot/AntA}/BP) - PPR_{Resp\ Rot/AntA}]*BP$$

$$Glycolytic\ reserve = Maximal\ glycolysis - Basal\ glycolysis$$

Where:

$BP\ (buffer\ power) = 0.05714$

$PPR_{Glyco} = PPR_{Total} - PPR_{Resp}$

$PPR_{Total} = ECAR_{Basal}/BP$

$ECAR_{Basal} = last\ ECAR\ measurement\ before\ the\ first\ injection$

$PPR_{Resp} = [10pH\text{-}pK1\ 37°C/(1+10pH\text{-}pK1\ 37°C)]x1xMitoOCR_{Basal}$

$pH = 7.4$

$pK1\ 37°C = 6.093$

ATP production parameters:

$$glycoATP = (PPR_{Glyco}x1) + MitoOCR_{Basal}x0.242x2$$

$$mitoATP = [(OCR_{ATP}x0.908)x2.486 + MitoOCR_{Basal}x0.121]x2$$

$$Total\ ATP = glycoATP + mitoATP$$

$$ATP\ production\ rate\ Index = glycoATP / mitoATP$$

To study the effect of Erdafitinib on functional metabolism, cells were treated for 24h before the assay with increasing concentrations of Erdafitinib (0.5, 5, 50, 500 nM), and a mito stress test assay was performed according to the manufacturer's instructions. Concentrations of the drugs

were the following: oligomycin 1 µM, FCCP 0.5 µM for RT112 and 5637 and 1 µM for UMUC3, HT1376 and J82 cell lines, Rotenone/Antimycin A 0.5 µM (both drugs).

NMR analysis (exo-metabolomics)

Culture preparation: $1.4x10^5$ cells/well were plated onto 6 well plates in maintenance medium. The next day, medium was changed to experimental medium (supplemented with 1 mM Na-Pyruvate), and cells were grown for 2 days. For data normalization, cells grown in parallel to samples for metabolomics were stained with Hoechst 33342 and nuclei counted with Operetta CLS™ and Harmony software, obtaining the starting and final numbers of cells.

Media collection: cell media were collected from each sample, centrifuged at 400g x 5 minutes, to remove residual cells and debris, and stored at -80°C until the NMR analysis. Blank media, at both the beginning and the end of the assay, were collected as well, and processed as cell media.

Samples for NMR analysis: samples were first thawed at 4 °C. Then, 600 µL of each cell culture medium were collected and mixed with 60 µL of Imidazole solution (1.095 mM final concentration in the NMR tube), serving as an internal standard and pH calibrator, along with 60 µL of D_2O. The final solution was then transferred to a 5 mm NMR tube for NMR acquisition.

Spectra acquisition: acquisition of ^{1}H-NMR spectra was performed using a Bruker Avance 700 MHz spectrometer (Billerica, MA, USA) equipped with SampleXpress Lite autosampler and Topspin software (version 2.1). The sequence used for acquiring each spectrum was a CPMG filter to reduce broad signals from proteins and lipids. The sequence used contains a water suppression with saturation pulses. Presaturation pulses in the sequence reduced the intensity of exchangeable protons (NH, OH), but their integrals were not used for absolute metabolite

quantification. Other acquisition parameters include temperature at 298K, 16 ppm spectral window, 128 scans, 4 dummy scans, 2-second relaxation delay, and 3-second acquisition time. The total duration of each experiment was 22 min.

Spectral analysis: metabolite identification and quantification were performed using Chenomx NMR Suite 8.5 (Chenomx Inc., Edmonton, AB, Canada). Spectra were processed with a 0.5 Hz line broadening, followed by manual phase and baseline correction. Signals were manually deconvoluted using the software's spectra database.

Measurement of the metabolite exchange rates: to properly evaluate variations in extracellular media metabolites due to intrinsic metabolism, metabolite exchange rates with the culture medium were evaluated by analysing the ratio between metabolite changes and the area under the cell growth curve.

Daily consumption or excretion of all quantified metabolites, $\Delta[M]_i^k$, was calculated after two days of culture and for all the replicates of the cell lines. The concentration differences were then converted into mass differences, $\Delta[m]_i^k$, by considering the total volume of the medium. This was done using the following equation (1):

$$\Delta[m]_i^k = ([M]_i^k - [M]_i^0) \cdot V$$

where $[M]_i^k$ refers to the concentration of the *i*-metabolite in the *k*-sample and $[M]_i^0$ to the concentration in the fresh medium cultured in the same condition. The area (A_c) under the growth curve for each cell line was calculated by integration between the starting (t_1) and final (t_2) times of culture, using the following equation (2):

$$A_c = \int_{t_1}^{t_2} n_0\, e^{k_c t}\, dt = \frac{n_0}{ln\ (n_2)\ - ln(n_0)} \left(\frac{n_2}{n_0} - 1\right)$$

where A_c refers to the area under the growth curve of cells, k_c is the exponential rate, n_0 is the initial number of cells, and n_2 is the number of cells after two days.

Metabolite exchange rates (ERs) were calculated using the following equation (3):

$$ER_i^k = \frac{\Delta[m]_i^k}{A_c}$$

LC-MS analysis (endo-metabolomics)

Culture preparation: 1.4x10^5 cells/well were plated onto 6 well plates in maintenance medium. The next day, medium was changed to experimental medium (supplemented with 1 mM Na-Pyruvate), and cells were grown for 2 days. For data normalization, cells grown in parallel to samples for metabolomics were stained with Hoechst 33342 and nuclei counted with Operetta CLS™ and Harmony software, obtaining the starting and final numbers of cells.

Metabolite extraction: cells were quickly rinsed with NaCl 0.9% and quenched with 500 µL ice-cold 70:30 acetonitrile:water. Plates were placed at -80 °C for 10 min, then cells were collected by scraping and sonicated 5 seconds for 5 pulses at 70% power twice. Samples were placed at -80 °C for 10 min and then sonicated 5 seconds for 5 pulses at 70% power twice. Samples were centrifuged at 12000g for 10 min and supernatants were collected in a glass insert and dried in a

centrifugal vacuum concentrator (Concentrator plus/Vacufuge plus, Eppendorf) at 30 °C for about 2.5 h. Samples were then resuspended with 150 µL H_2O prior to analyses.

LC-MS analysis: LC separation was performed using an Agilent 1290 Infinity UHPLC system and an InfintyLab Poroshell 120 PFP column (2.1 × 100 mm, 2.7 µm; Agilent Technologies). Mobile phase A was water with 0.1% formic acid. Mobile phase B was acetonitrile with 0.1% formic acid. The injection volume was 10 µL and LC gradient conditions were: 0 min: 100% A; 2 min: 100% A; 4 min: 99% A; 10 min: 98% A; 11 min: 70% A; 15 min: 70% A; 16 min: 100% A with 2 min of post-run. Flow rate was 0.2 ml/ min and column temperature was 35 °C. MS detection was performed using an Agilent 6550 iFunnel Q-TOF mass spectrometer with Dual JetStream source operating in negative ionization mode. MS parameters were: gas temp: 285 °C; gas flow: 14 l/min; nebulizer pressure: 45 psig; sheath gas temp: 330 °C; sheath gas flow: 12 l/min; VCap: 3700 V; Fragmentor: 175 V; Skimmer: 65 V; Octopole RF: 750 V. Active reference mass correction was done through a second nebulizer using masses with *m*/*z*: 112.9855 and 1033.9881. Data were acquired from *m*/*z* 60–1050. Data analysis and isotopic natural abundance correction were performed using MassHunter Profinder (version 10.0.2). Data preprocessing was performed using the Batch Targeted Feature Extraction algorithm and Agile 2 algorithm. This software assigned identities to metabolites by searching against an in-house compound database built with Agilent PCDL Manager (version B.08.00) based on the metabolite formula and its corresponding retention time with a score > 75. Peak areas were normalized for cell number for each sample, as explained above.

Data analysis: data were analysed using MetaboAnalyst 6.0 online tool (https://www.metaboanalyst.ca/). A statistical analysis [one factor] was performed to generate the heatmap for *FGFR3*-altered vs *FGFR3*-wt comparison. For this analysis, data were processed as follows. As default suggestion by the tool, features with >50% of missing data were removed. The remaining missing values were replaced by LoDs (1/5 of the minimum positive value of each variable). The interquartile range (IQR) was selected as statistical filter. Samples were normalized by Log transformation (base 10) and scaled using Pareto scaling. Significative metabolites (FDR-adj p val<0.05) were selected for the heatmap. Comparisons of each metabolite were performed calculating mean and standard deviation of the two groups, considering each missing value as 0, and graphing each metabolite cell-normalized mean peak intensities using GraphPad Prism software. Quantitative enrichment analyses were performed using MetaboAnalyst 6.0 online tool, using the complete metabolite lists, with relative peak intensities, for the online analysis.

Glycolytic flux measurement

Cells were seeded onto CellCarrier-96 Ultra Microplates 96-well (PerkinElmer) in maintenance medium at cell density of 1.5 x 10^4 cells/well and incubated overnight at 37 °C and 5% CO_2. The day after seeding, the medium was replaced with 90 µL/well of experimental medium, and transfection with CMV-Hylight Biosensor, a fluorescent biosensor for fructose 1,6-bisphosphate (FBP) where changes in FBP concentration strongly correlate with changes in glycolytic flux, was performed following the authors' instructions[40]. CMV-Hylight plasmid was deposited by Richard Goodman's lab and purchased from Addgene (Addgene plasmid # 193447; http://n2t.net/addgene:193447; RRID:Addgene 193447). Cells were transfected using TransIT-X2® Dynamic Delivery System (Mirus Bio), following the manufacturer's instructions. After 48

hours post-transfection, cells were stained with Hoechst 33342 (working concentration 1 µg/mL, incubated for 15 min at 37 °C and 5% CO_2), and counted to calculate the transfection efficiency using Harmony software. Transfection efficiency (%) was calculated as: (Number of Hylight-positive cells / Total number of nuclei) ×100.

Hylight Biosensor acquisition was obtained using two different settings:

1. Excitation 390−420 nm, emission 500−550 nm (excitation at 405 nm results in stronger emission when FBP is not bound to the biosensor).
2. Excitation 460−490 nm, emission 500−550 nm (excitation at 488 nm results in stronger emission when FBP is bound to the biosensor).

The transfection efficiency % variates from 0.5% (J82) to 40% (5637) depending on the cell line. After 72 hours post-transfection, glycolytic flux measurement was performed (on a parallel set of cells not used for transfection efficiency assessment) as follows: cells were washed with D-PBS containing Ca^{2+} and Mg^{2+}, then they were starved for 1 hour in experimental medium without glucose (0 mM) at 37 °C and 5% CO_2. Images (16 frames/well) were acquired at 40x magnification using Operetta CLS™, using the same two-excitations settings reported above. Then, 10 µL/well of D-(+)-Glucose (Sigma, Cat.G8769) 100 mM was added to 90 µl/well to each well to reach the final concentration of 10 mM glucose. Cells were acquired 5 minutes after glucose addition. The same procedure was followed for the addition of oligomycin A (Sigma, Cat.75351) at final concentration 2.5 µM and 2-Deoxy-D-glucose (2-DG, Santa Cruz Biotechnology CAS 154-17-6) at final concentration 50 mM. The normalized glycolytic flux was measured as $(R_x - R_0)/R_0$, where R_x is the ratio of mean fluorescence intensity of the Hylight biosensor at ex 488 nm / ex 405 nm ($R = F_{488}/F_{405}$) at timepoint *X*, and R_0 is the same ratio calculated at 0 mM glucose (baseline). The calculation was performed after selecting the population of transfected cells.

Transcriptomics Analysis

Culture preparation: 1.4x10^5 cells/well were plated onto 6 well plates in maintenance medium. The next day, medium was changed to experimental medium, and cells were grown for 2 days.

Sample collection, RNA extraction and digestion with DNase: cells were washed with PBS and harvested adding 1 mL/well of TRI Reagent™ Solution (AM9738, Invitrogen™-Thermo Fisher Scientific) to lyse cells. Cell lysates of two wells were pooled. RNA was separated from DNA and proteins adding 200 µL/tube chloroform. After 7 minutes of incubation at RT, samples were centrifuged (18000g x 15 mins at 4°C). The aqueous phase was transferred to a new tube, adding 500 µL of 2-propanol, and centrifuged again. Supernatants were separated from pellets (RNA precipitate) and 1 mL of 75% ethanol was added. Another centrifugation was performed (18000g x 10 mins at 4°C), and RNA-containing pellet was resuspended in 100 µL of RNase-free water. RNA solutions were purified using RNeasy Mini Kit (74104, Qiagen) and treated with DNase, following manufacturer's instructions.

RNA purity was tested using NanoDrop™ One/OneC Microvolume UV-Vis Spectrophotometer (Thermo Scientific™).

RNA sequencing analysis: RNA-Seq was performed using Illumina NovaSeq 6000, with an average of 60 million of uniquely mapped reads per sample. Raw sequences were initially tested using FastQC (https://www.bioinformatics.babraham.ac.uk/projects/fastqc/). Subsequently, fastq reads were aligned using GRCh38/hg38 as the reference human genome with the splice-aware aligner Star[75] and the quantMode GeneCounts parameter. Bam alignment files were indexed using Samtools[76]. The sorted, indexed bam alignment files, together with bai indexes, were

subsequently used for manual inspection of the aligned data using the Integrative Genomics Viewer[77].

Computational Analysis

Starting from omics data, computational analysis and integration was performed. In addition to transcriptomic data from our cell lines panel, two more datasets were considered and analysed.

CCLE dataset was downloaded from https://sites.broadinstitute.org/ccle; the dataset was filtered to retain the cell lines of interest and with available metadata for accurate comparison being *FGFR3*-altered (6 cell lines) vs *FGFR3*-wt (11 cell lines). In detail, among all the cell lines in this dataset, we selected all the cell lines with "bladder" as site subtype, obtaining a list of 25 cell lines. We then excluded the HS172T cell line, as they are classified as fibroblast cell line. SCaBER cell line was excluded as it is established from a squamous cell carcinoma. We excluded 253J, 253J-BV and UMUC1 cell lines as they represent metastatic stages. We finally excluded KMBC2, SW1710, and VMCUB1 cell lines as the complete classification in terms of stage and grade is not defined. We obtained a list of 11 cell lines presenting the wt form of FGFR3 (5637, BC3C, BFTC905, CAL29, HT1376, JMSU1, KU1919, T24, TCCSUP, UBLC1, and UMUC3 cell lines), and 6 cell lines sharing an activating mutation of this gene (647V, HT1197, J82, RT112, RT4, and SW780 cell lines).

TCGA Dataset (Cell 2017[50]) was downloaded from https://www.cancer.gov using TCGAbiolinks package (v2.38.0)[78]. The dataset was filtered to retain only BLCA patient samples, for a total of 57 *FGFR3*-altered and 351 *FGFR3*-wt MIBC samples.

Batch correction and data normalization

To evaluate the explanatory strength of *FGFR3* alterations, a variance partition analysis (VPA)[79] was performed across all datasets. The analysis revealed a modest effect size, suggesting that other covariates are contributing substantially to the observed variance. This outcome underscores the necessity for careful statistical control in subsequent analyses.

Differential expression analysis for lab cell lines was conducted by building a simple design matrix, just considering condition (*FGFR3* mutational status: altered vs wild-type); given the reduced cell line panel no other variables were considered within the contrast matrix to avoid overcorrection due to collinearity between independent covariates.

CCLE dataset, retained 17 cell lines after manual curation. Given the larger number of lines and since VPA revealed a moderate variance explanatory power for *FGFR3* as variable of interest, a Surrogate Variable Analysis[80] shall be performed to mitigate the masking effect for other confounding factors so to extract clean and meaningful results from DEA and GSEA. Invasiveness (stage), since a co-variate of interest and since its explained variance surpass *FGFR3* will be kept as random effect for modelling. Leek method was applied to extract 1 surrogate variable (SV) as the optimal number.

TCGA dataset also required batch correction given highly plausible patient variability, thus the same approach was employed for consistency across analyses; Leek method was applied and determined 1 surrogate variable as the optimal number. The SV was then incorporated into the contrast matrix before proceeding with differential expression analysis.

Raw counts for all experimental conditions were subsequently normalized following the standard DESeq2 workflow to account for sequencing depth and RNA composition (see following paragraph).

Differential Expression Analysis

Differential expression analysis between *FGFR3*-altered and *FGFR3*-wt samples, for the three experimental groups described above, was performed using the DESeq2 package (v3.21) in R (v4.5.2)[81].

Genes with fewer than 10 total counts across the smallest experimental group were filtered out prior to analysis. The Wald test was employed for hypothesis testing using parametric dispersion estimates. The wild-type condition was set as the reference level for comparison (i.e. *FGFR3*-altered vs *FGFR3*-wt).

Log2 fold changes were shrunk using the apeglm adaptive shrinkage estimator to improve effect size estimates for genes with low counts or high dispersion[82]. Multiple testing correction was applied using the Benjamini-Hochberg procedure, with adjusted p-values < 0.05 considered statistically significant. Normalized count, calculated by adjusting raw counts by DESeq2 median of ratios, were extracted using the counts (dds, normalized = TRUE) function for downstream visualization and reporting.

For gene set enrichment analysis (GSEA), a ranking metric has been defined as the product of the shrunken log2 fold change and the negative logarithm of the adjusted p-value:

$$rnk_i = \log_2 FoldChange_i * (-\log_{10} P.Adjusted_i), \forall i \in \mathrm{I}$$

where I is the gene set

Gene Set Enrichment Analysis Preparation

For GSEA, a pre-ranked gene list was generated by ordering all genes based on the computed ranking metric, as described above, in descending order. This ranked list file was exported for use with GSEA software[83]. HALLMARK 50 Gene Sets (v2026) have been used to investigate the top enriched cellular processes. Normalized enrichment scores (NES) have been used for visually representing GSEA results.

Reproducibility: to ensure full computational reproducibility, all R package versions and dependencies were tracked using renv[84]. The complete analysis environment can be restored using the provided renv.lock file. The complete analysis workflow, related scripts and basic visualization plot are publicly available at the link reported in “Data availability” section.

Reaction Activity Scores

To properly assess the possible impact of the transcriptomics data on metabolism, in addition to the classical gene set enrichment analysis, we performed a statistical analysis of the Reaction Activity Scores (RAS)[85].

These features are derived by mapping the gene expression data to a set of metabolic reactions, organized in a metabolic network model, by means of the Gene Protein Reaction (GPR) rules. These rules describe the relationship between genes and reactions and among genes possibly associated with the same reaction. Specifically, the GPRs represent logical formulas describing how gene products concur to catalyse a given reaction, using Boolean operators. The AND operator is used when distinct genes encode different subunits of the same enzyme, whereas the OR operator is used for genes encoding isoforms of the same enzyme. These AND and OR

operators can be combined to describe more complex scenarios involving both isoforms and subunits.

The RAS scores are calculated by substituting the mRNA abundances in the corresponding GPRs. Then, the logical expressions are solved by taking the minimum transcript level value when multiple genes are joined by an AND operator, and the sum of their values when multiple genes are joined by an OR operator. In the case of GPRs combining both operators, we respected their standard precedence. Moreover, in case of missing expression value, we decided to solve the rule "A AND NaN" as A and the rule "A OR NaN" as A.

Using the RAS scores, starting from a set of transcriptomics profiles, we can generate a set of metabolic profiles, each one consisting of a selected number of RAS scores, each specific for a metabolic reaction.

The metabolic network model

To properly analyse the fluxomics difference between the cell lines, we used the recently published metabolic network model ENGRO2[47]. ENGRO2 contains 469 reactions, 395 metabolites, and 498 genes and represents a follow-up of the core model of human central metabolism ENGRO1[86]. For this model, 351 model reactions are associated with a gene-protein-reaction (GPR) rule. More in detail, there are 200 single-gene GPRs, 98 OR-expression, 17 AND-expression, and 29 complex rules (i.e., logical expression with both AND or OR operator). With this model, we can study the possible implications of transcriptomics and exometabolomics on a selected number of metabolic pathways involved in human central carbon and essential amino acids metabolism. Moreover, for this model, a manually-curated map (see ***Supplementary Fig.***

7b) is available for mapping statistically significant differences between the RAS and fluxes of two groups of samples. For the RASs mapping (***Fig 6b, Supplementary Fig. 4b and 5***), selection of the significant reactions to be mapped was performed on p-value and Z-score, or fold-change directly. The formula used to calculate z-score is reported below:

$$\frac{\mu_1 - \mu_2}{\sqrt{\frac{\sigma_1}{n_1} - \frac{\sigma_2}{n_2}}}$$

where μ_1 ,μ_2 are the average RAS for the two groups, σ_1 ,σ_2 the standard deviations, and n_1 ,n_2 the size of the populations.

Regarding the mapping of simulated fluxes (***Fig. 5b***), we simulated a growth medium condition in which exogenous metabolites are abundantly available, or possible constrained by exometabolomics. Exogenous metabolites in the ENGRO2 network include glucose, lactate, oxygen, water, hydrogen, folic acid, and all essential and non-essential amino acids.

From ENGRO2 to cell-relative constraint-based models

To predict the differences in the fluxes of the five cell lines studied, we used constraint-based modelling (CBM). CBM is based on a steady state assumption for internal metabolites. Given a *M* × *N* stoichiometric matrix S, with M metabolites and N reactions, and a flux vector ***v***, the steady-state assumption imposes that $S \cdot \boldsymbol{v} = 0$. To mimic as closely as possible the biological process in analysis, we constraint the space of feasible fluxes by means of specific vectors ***vL*** and ***vU***, which specify the lower and upper bounds for the components of the flux vector ***v***, respectively. These bounds are set according to the differences observed in the experimental datasets, i.e. transcriptomics and exometabolomics. We distinguished two types of constraints:

- **Constraints on exchange fluxes**: we set these constraints according to the experimentally determined fluxes of lactate, glucose, pyruvate, non-essential and essential amino acids. Specifically, the two values of the exometabolomics (i.e. the two biological replicates) are used as upper and lower bound of the corresponding exchange reactions.

- **Constraints on internal reactions**: we set these constraints according to the RAS value. Assuming that a cell with lower enzyme activity for a given internal reaction *r* has in principle a lower capability to carry flux through such reaction, we constrained the maximum and minimum flux bound ***vLc*** and ***vUc*** of a given cell-line *c* as follows:

$$vUrc < \frac{RASrc}{maxcRASrc} * maxUc$$

where $RASrc$ is the RAS value of a given reaction *r* and a cell-line *c*. Note that if the RAS value of a reaction is 0, the corresponding flux is constrained to 0. When the RAS value is different from 0, the reaction can (but it is not obliged) assume a flux different from zero.

Once the five different metabolic networks are created, 10,000 possible flux distributions are obtained for each network, by uniformly sampling the feasible flux region of each metabolic model. Finally, we performed a Metabolic Flux Enrichment Analysis to compare the fluxes between the two groups of samples, using the Mann-Whitney U-test to identify statistically significant differences and the fold change is calculated considering the difference between means normalized by the absolute value of the sum. In this way, we always obtain a value between -1 and 1.

Statistics and Reproducibility

Unless otherwise specified, all experiments were carried out at least in biological triplicate. The number of technical replicates within each experiment is reported for each assay in figure legends. Results were expressed as means ± standard deviation and variables were compared using unpaired Student's t-test, ordinary One-Way ANOVA, Two-Way ANOVA, or general linear model according to their distribution. A p-value < 0.05 was considered statistically significant. All statistical analyses were performed using GraphPad version 10 (GraphPad Software, Inc., San Diego, CA, USA) software.

Data Normalization and Scaling

To ensure equal contribution of all features to clustering, Unit-Variation scaling was applied to the absolute values of the exchange rates and the Seahorse parameters.

Hierarchical Clustering and Heatmap Generation

A hierarchical unsupervised clustering heatmap was generated in R using the heatmaply package. Clustering was performed using Euclidean distance as the similarity metric and complete linkage as the agglomeration method. The heatmap was visualized as an interactive plot with a colour scale ranging from blue (low relative exchange rates) to red (high relative exchange rates).

Supervised multivariate model

The multivariate analysis of the data was carried out using SIMCA (version 17, Sartorius). The classification model was built using Orthogonal PLS Modelling (OPLS) in the discriminant version (OPLS-DA). The variables were the different ERs calculated from Equation (3) and the variables of

the Seahorse analyses. All data were normalized using probabilistic quotients 3 and Unit-Variation scaled.

We use Variable Importance in the Projection (VIP) to identify metabolites mainly responsible for the difference. Additionally, ANOVA of the cross-validated residual (CV ANOVA) test was performed to evaluate the significance of the multivariate model. All these parameters were calculated using SIMCA.

Data availability

All the numerical source raw data are available in the "Supplementary Data" file.

The exometabolomic and endometabolomic data can be obtained at the following link:

https://osf.io/z5fe9/overview?view_only=596e2b3900b445eab3790d67c38e8673

The transcriptomic data can be obtained at the following link:

https://www.ncbi.nlm.nih.gov/sra/PRJNA1253429

Code availability

All the scripts used for differential expression analysis and GSEA analysis can be obtained at the following link:

https://github.com/SimonePonzetto/Ducci.et.al_CommsBiol.2026

All the scripts used for the *in-silico* fluxomics computation are available at:

https://github.com/CompBtBs/BladderCancer_FGFR3

Acknowledgements

The authors would like to thank Fondazione Umberto Veronesi for supporting G.D. through 2025 scholarship. The authors would also like to thank SYSBIO/ISBE.IT Center of Systems Biology, particularly Professor Lilia Alberghina, and the Project of Excellence CHRONOS (CHRonical multifactorial disorders explored by NOvel integrated Strategies) of the Department of Biotechnology and Biosciences, University of Milano-Bicocca, for providing advanced technologies used in this study. The authors acknowledge the support of the PROPOSTA PROGETTUALE IR0000010 ELIXIRxNEXTgenIT-ELIXIR x NextGenerationIT: Consolidamento dell'Infrastruttura Italiana per i Dati Omici e la Bioinformatica-ElixirxNextGenIT"—CUP B53C22001800006, for providing the strategic infrastructure for omics data and bioinformatics. R.P. acknowledges the support of the Italian MUR Dipartimenti di Eccellenza 2023-2027 (l. 232/2016, art. 1, commi 314 - 337).

Some images in the graphical abstract has been provided by Servier Medical Art (https://smart.servier.com), licensed under CC BY 4.0 (https://creativecommons.org/licenses/by/4.0/). Original elements were customised and adapted for the final composition, including modifications to color, scaling and cropping.

Declaration of generative AI and AI-assisted technologies in the writing process: during the preparation of this work, the authors used ChatGPT to improve the language and readability of some sentences of the manuscript. After using this tool, the authors reviewed and edited the content as needed and take full responsibility for the content of the publication.

Funding

E.S. and M.V. disclose support for the research of this work from the Italian Ministry of University and Research (MIUR) (Research facilitation fund - Fondo per le Agevolazioni alla Ricerca—FAR). M.V. discloses support for the research of this work from the European Union's Horizon 2020 research and innovation programme (grant agreement No 871277). E.S. through Department of Biotechnology and Biosciences, and R.P. through Department of Medicine and Surgery, University of Milano-Bicocca, disclose support for the research of this work from the European Union - NextGenerationEU through the Italian Ministry of University and Research (PNRR - M4C2-I1.3 Project PE_00000019 "HEAL ITALIA"). DO.C. discloses support for the research of this work from Collezione Nazionale di Composti Chimici e Centro Screening (CNCCS) Consortium, Project B, Sp2, WP9 "Metabolomica.

Author Contributions

Conceptualization: E.S., G.P. and M.V.; data curation and investigation in morpho-functional and seahorse metabolic analyses: G.D., V.P., G.G., GL.C., D.B., V.S., E.V.; data curation and investigation in exometabolomic analysis: G.C., G.P.; data curation and investigation in transcriptomic analysis: D.D., S.S., S.P.; data curation and investigation in endometabolomic analysis: M.B., D.G.; data integration and mathematical modelling: G.D., S.P., B.G., C.D.; supervision and data discussion: E.S., G.P., G.D., G.C., M.V., A.M., R.P., D.O.C., C.R., R.V. and A.G.; funding acquisition: M.V., E.S., R.P. and D.O.C.; writing—original draft: E.S., G.D. and G.P.; writing—review & editing: E.S., G.P., G.D., M.V., A.M., R.P. and D.O.C.

All authors have read and agreed to the published version of the manuscript.

Competing interests

The authors declare no competing interests.

References

1. Bray, F. *et al.* Global cancer statistics 2022: GLOBOCAN estimates of incidence and mortality worldwide for 36 cancers in 185 countries. *CA. Cancer J. Clin.* **74**, 229–263 (2024).

2. Kaufman, D. S., Shipley, W. U. & Feldman, A. S. Bladder cancer. *Lancet (London, England)* **374**, 239–49 (2009).

3. Down, C. J., Nair, R. & Thurairaja, R. Bladder cancer. *Surg.* **34**, 532–539 (2016).

4. Fujii, Y. Prediction models for progression of non-muscle-invasive bladder cancer: A review. *Int. J. Urol.* **25**, 212–218 (2018).

5. Li, R. *et al.* FGFR Inhibition in Urothelial Carcinoma. *Eur. Urol.* **87**, 110–122 (2025).

6. Tran, L., Xiao, J.-F., Agarwal, N., Duex, J. E. & Theodorescu, D. Advances in bladder cancer biology and therapy. *Nat. Rev. Cancer* **21**, 104–121 (2021).

7. Dyrskjøt, L. *et al.* Bladder cancer. *Nat. Rev. Dis. Prim.* **9**, 58 (2023).

8. Guo, G. *et al.* Whole-genome and whole-exome sequencing of bladder cancer identifies frequent alterations in genes involved in sister chromatid cohesion and segregation. *Nat. Genet.* **45**, 1459–1463 (2013).

9. Thomas, J. & Sonpavde, G. Molecularly Targeted Therapy towards Genetic Alterations in

Advanced Bladder Cancer. *Cancers (Basel).* **14**, 1795 (2022).

10. Szklener, K., Chmiel, P., Michalski, A. & Mańdziuk, S. New Directions and Challenges in Targeted Therapies of Advanced Bladder Cancer: The Role of FGFR Inhibitors. *Cancers (Basel).* **14**, 1416 (2022).

11. Hahn, N. M. *et al.* A Phase II Trial of Dovitinib in BCG-Unresponsive Urothelial Carcinoma with FGFR3 Mutations or Overexpression: Hoosier Cancer Research Network Trial HCRN 12-157. *Clin. Cancer Res.* **23**, 3003–3011 (2017).

12. Milowsky, M. I. *et al.* Phase 2 trial of dovitinib in patients with progressive FGFR3-mutated or FGFR3 wild-type advanced urothelial carcinoma. *Eur. J. Cancer* **50**, 3145–3152 (2014).

13. Loriot, Y. *et al.* Erdafitinib in Locally Advanced or Metastatic Urothelial Carcinoma. *N. Engl. J. Med.* **381**, 338–348 (2019).

14. Herrera-Abreu, M. T. *et al.* Parallel RNA Interference Screens Identify EGFR Activation as an Escape Mechanism in FGFR3 -Mutant Cancer. *Cancer Discov.* **3**, 1058–1071 (2013).

15. Wang, Z., Muthusamy, V., Petrylak, D. P. & Anderson, K. S. Tackling FGFR3-driven bladder cancer with a promising synergistic FGFR/HDAC targeted therapy. *npj Precis. Oncol.* **7**, 70 (2023).

16. Sternberg, C. N. *et al.* FORT-1: Phase II/III Study of Rogaratinib Versus Chemotherapy in Patients With Locally Advanced or Metastatic Urothelial Carcinoma Selected Based on FGFR1 / 3 mRNA Expression. *J. Clin. Oncol.* **41**, 629–639 (2023).

17. Liu, P. C. C. *et al.* INCB054828 (pemigatinib), a potent and selective inhibitor of fibroblast

growth factor receptors 1, 2, and 3, displays activity against genetically defined tumor models. *PLoS One* **15**, e0231877 (2020).

18. Subbiah, V. *et al.* FIGHT-101, a first-in-human study of potent and selective FGFR 1-3 inhibitor pemigatinib in pan-cancer patients with FGF/FGFR alterations and advanced malignancies. *Ann. Oncol.* **33**, 522–533 (2022).

19. Ascione, C. M. *et al.* Role of FGFR3 in bladder cancer: Treatment landscape and future challenges. *Cancer Treat. Rev.* **115**, 102530 (2023).

20. Hanahan, D. Hallmarks of Cancer: New Dimensions. *Cancer Discov.* **12**, 31–46 (2022).

21. Woolbright, B. L., Ayres, M. & Taylor, J. A. Metabolic changes in bladder cancer. *Urol. Oncol. Semin. Orig. Investig.* **36**, 327–337 (2018).

22. Warburg, O. On the Origin of Cancer Cells. *Science (80-.).* **123**, 309–314 (1956).

23. Vander Heiden, M. G., Cantley, L. C. & Thompson, C. B. Understanding the Warburg Effect: The Metabolic Requirements of Cell Proliferation. *Science (80-.).* **324**, 1029–1033 (2009).

24. Alberghina, L. The Warburg Effect Explained: Integration of Enhanced Glycolysis with Heterogeneous Mitochondria to Promote Cancer Cell Proliferation. *Int. J. Mol. Sci.* **24**, 15787 (2023).

25. Patra, K. C. & Hay, N. The pentose phosphate pathway and cancer. *Trends Biochem. Sci.* **39**, 347–54 (2014).

26. Yoo, H. C., Yu, Y. C., Sung, Y. & Han, J. M. Glutamine reliance in cell metabolism. *Exp. Mol. Med.* **52**, 1496–1516 (2020).

27. Koundouros, N. & Poulogiannis, G. Reprogramming of fatty acid metabolism in cancer. *Br. J. Cancer* **122**, 4–22 (2020).

28. Panieri, E. & Santoro, M. M. ROS homeostasis and metabolism: a dangerous liason in cancer cells. *Cell Death Dis.* **7**, e2253–e2253 (2016).

29. Boroughs, L. K. & DeBerardinis, R. J. Metabolic pathways promoting cancer cell survival and growth. *Nat. Cell Biol.* **17**, 351–359 (2015).

30. Kroemer, G. & Pouyssegur, J. Tumor Cell Metabolism: Cancer's Achilles' Heel. *Cancer Cell* **13**, 472–482 (2008).

31. Hanahan, D. & Weinberg, R. A. Hallmarks of cancer: The next generation. *Cell* **144**, 646–674 (2011).

32. Iurlaro, R., León-Annicchiarico, C. L. & Muñoz-Pinedo, C. Regulation of Cancer Metabolism by Oncogenes and Tumor Suppressors. in 59–80 (2014). doi:10.1016/B978-0-12-416618-9.00003-0.

33. Nagarajan, A., Malvi, P. & Wajapeyee, N. Oncogene-Directed Alterations in Cancer Cell Metabolism. *Trends in Cancer* **2**, 365–377 (2016).

34. Lee, S. Y. *et al.* Oncogenic Metabolism Acts as a Prerequisite Step for Induction of Cancer Metastasis and Cancer Stem Cell Phenotype. *Oxid. Med. Cell. Longev.* **2018**, (2018).

35. Navarro, C. *et al.* Metabolic Reprogramming in Cancer Cells: Emerging Molecular Mechanisms and Novel Therapeutic Approaches. *Pharmaceutics* **14**, 1303 (2022).

36. Xiao, Y. *et al.* Emerging therapies in cancer metabolism. *Cell Metab.* **35**, 1283–1303 (2023).

37. Lemberg, K. M., Gori, S. S., Tsukamoto, T., Rais, R. & Slusher, B. S. Clinical development of metabolic inhibitors for oncology. *J. Clin. Invest.* **132**, (2022).

38. Dolfi, S. C. *et al.* The metabolic demands of cancer cells are coupled to their size and protein synthesis rates. *Cancer Metab.* **1**, 20 (2013).

39. D'Aloia, A. *et al.* RalGPS2 Interacts with Akt and PDK1 Promoting Tunneling Nanotubes Formation in Bladder Cancer and Kidney Cells Microenvironment. *Cancers (Basel).* **13**, 6330 (2021).

40. Koberstein, J. N. *et al.* Monitoring glycolytic dynamics in single cells using a fluorescent biosensor for fructose 1,6-bisphosphate. *Proc. Natl. Acad. Sci.* **119**, (2022).

41. Cassim, S., Vučetić, M., Ždralević, M. & Pouyssegur, J. Warburg and Beyond: The Power of Mitochondrial Metabolism to Collaborate or Replace Fermentative Glycolysis in Cancer. *Cancers (Basel).* **12**, 1119 (2020).

42. Petrella, G., Ciufolini, G., Vago, R. & Cicero, D. O. The Interplay between Oxidative Phosphorylation and Glycolysis as a Potential Marker of Bladder Cancer Progression. *Int. J. Mol. Sci.* **21**, 8107 (2020).

43. Matés, J. M., Campos-Sandoval, J. A., de los Santos-Jiménez, J. & Márquez, J. Glutaminases regulate glutathione and oxidative stress in cancer. *Arch. Toxicol.* **94**, 2603–2623 (2020).

44. Guo, W. *et al.* Dysregulated Glutamate Transporter SLC1A1 Propels Cystine Uptake via Xc− for Glutathione Synthesis in Lung Cancer. *Cancer Res.* **81**, 552–566 (2021).

45. Locasale, J. W. Serine, glycine and one-carbon units: cancer metabolism in full circle. *Nat.*

Rev. Cancer **13**, 572–583 (2013).

46. Li, A. M. & Ye, J. Reprogramming of serine, glycine and one-carbon metabolism in cancer. *Biochim. Biophys. Acta - Mol. Basis Dis.* **1866**, 165841 (2020).

47. Di Filippo, M. *et al.* INTEGRATE: Model-based multi-omics data integration to characterize multi-level metabolic regulation. *PLOS Comput. Biol.* **18**, e1009337 (2022).

48. Damiani, C. *et al.* A metabolic core model elucidates how enhanced utilization of glucose and glutamine, with enhanced glutamine-dependent lactate production, promotes cancer cell growth: The WarburQ effect. *PLoS Comput. Biol.* **13**, 1–29 (2017).

49. Galuzzi, B. G., Vanoni, M. & Damiani, C. Combining denoising of RNA-seq data and flux balance analysis for cluster analysis of single cells. *BMC Bioinformatics* **23**, 445 (2022).

50. Robertson, A. G. *et al.* Comprehensive Molecular Characterization of Muscle-Invasive Bladder Cancer. *Cell* **171**, 540-556.e25 (2017).

51. Lamont, F. R. *et al.* Small molecule FGF receptor inhibitors block FGFR-dependent urothelial carcinoma growth in vitro and in vivo. *Br. J. Cancer* **104**, 75–82 (2010).

52. Siracusano, S., Rizzetto, R. & Porcaro, A. B. Bladder cancer genomics. *Urol. J.* **87**, 49–56 (2020).

53. Audenet, F., Attalla, K. & Sfakianos, J. P. The evolution of bladder cancer genomics: What have we learned and how can we use it? *Urol. Oncol. Semin. Orig. Investig.* **36**, 313–320 (2018).

54. Bogale, D. E. The roles of FGFR3 and c-MYC in urothelial bladder cancer. *Discov. Oncol.* **15**,

295 (2024).

55. Faubert, B., Solmonson, A. & DeBerardinis, R. J. Metabolic reprogramming and cancer progression. *Science (80-.).* **368**, (2020).

56. Liaghat, M. *et al.* The impact of epithelial-mesenchymal transition (EMT) induced by metabolic processes and intracellular signaling pathways on chemo-resistance, metastasis, and recurrence in solid tumors. *Cell Commun. Signal.* **22**, 575 (2024).

57. Sciacovelli, M. & Frezza, C. Metabolic reprogramming and epithelial-to-mesenchymal transition in cancer. *FEBS J.* **284**, 3132–3144 (2017).

58. Raggi, C. *et al.* Mitochondrial oxidative metabolism contributes to a cancer stem cell phenotype in cholangiocarcinoma. *J. Hepatol.* **74**, 1373–1385 (2021).

59. de Visser, K. E. & Joyce, J. A. The evolving tumor microenvironment: From cancer initiation to metastatic outgrowth. *Cancer Cell* **41**, 374–403 (2023).

60. Agarwala, Y., Brauns, T. A., Sluder, A. E., Poznansky, M. C. & Gemechu, Y. Targeting metabolic pathways to counter cancer immunotherapy resistance. *Trends Immunol.* **45**, 486–494 (2024).

61. Denise, C. *et al.* 5-Fluorouracil resistant colon cancer cells are addicted to OXPHOS to survive and enhance stem-like traits. *Oncotarget* **6**, 41706–41721 (2015).

62. Damiani, C., Gaglio, D., Sacco, E., Alberghina, L. & Vanoni, M. Systems metabolomics: from metabolomic snapshots to design principles. *Curr. Opin. Biotechnol.* **63**, 190–199 (2020).

63. Shah, R. & Chen, S. Metabolic Signaling Cascades Prompted by Glutaminolysis in Cancer.

Cancers (Basel). **12**, 2624 (2020).

64. Tufail, M., Jiang, C.-H. & Li, N. Altered metabolism in cancer: insights into energy pathways and therapeutic targets. *Mol. Cancer* **23**, 203 (2024).

65. Pan, S., Fan, M., Liu, Z., Li, X. & Wang, H. Serine, glycine and one-carbon metabolism in cancer (Review). *Int. J. Oncol.* **58**, 158–170 (2020).

66. Marchetti, P., Fovez, Q., Germain, N., Khamari, R. & Kluza, J. Mitochondrial spare respiratory capacity: Mechanisms, regulation, and significance in non-transformed and cancer cells. *FASEB J.* **34**, 13106–13124 (2020).

67. Kacew, A. & Sweis, R. F. FGFR3 Alterations in the Era of Immunotherapy for Urothelial Bladder Cancer. *Front. Immunol.* **11**, (2020).

68. Kamitani, R. *et al.* Tumor immune microenvironment dynamics and outcomes of prognosis in non-muscle-invasive bladder cancer. *Cancer Sci.* **115**, 3963–3972 (2024).

69. Liu, L. *et al.* KDM6A-ARHGDIB axis blocks metastasis of bladder cancer by inhibiting Rac1. 1–21 (2021).

70. Pang, K. *et al.* The ERH gene regulates migration and invasion in 5637 and T24 bladder cancer cells. 1–12 (2019).

71. Pasquale, V. *et al.* Profiling and Targeting of Energy and Redox Metabolism in Grade 2 Bladder Cancer Cells with Different Invasiveness Properties. *Cells* **9**, 1–26 (2020).

72. Campioni, G. *et al.* An Optimized Workflow for the Analysis of Metabolic Fluxes in Cancer Spheroids Using Seahorse Technology. *Cells* **11**, 866 (2022).

73. Mookerjee, S. A., Goncalves, R. L. S., Gerencser, A. A., Nicholls, D. G. & Brand, M. D. The contributions of respiration and glycolysis to extracellular acid production. *Biochim. Biophys. Acta - Bioenerg.* **1847**, 171–181 (2015).

74. Mookerjee, S. A., Gerencser, A. A., Nicholls, D. G. & Brand, M. D. Quantifying intracellular rates of glycolytic and oxidative ATP production and consumption using extracellular flux measurements. *J. Biol. Chem.* **292**, 7189–7207 (2017).

75. Dobin, A. *et al.* STAR: Ultrafast universal RNA-seq aligner. *Bioinformatics* **29**, 15–21 (2013).

76. Danecek, P. *et al.* Twelve years of SAMtools and BCFtools. *Gigascience* **10**, (2021).

77. Thorvaldsdóttir, H., Robinson, J. T. & Mesirov, J. P. Integrative Genomics Viewer (IGV): High-performance genomics data visualization and exploration. *Brief. Bioinform.* **14**, 178–192 (2013).

78. Colaprico, A. *et al.* TCGAbiolinks: an R/Bioconductor package for integrative analysis of TCGA data. *Nucleic Acids Res.* **44**, e71–e71 (2016).

79. Hoffman, G. E. & Schadt, E. E. variancePartition: interpreting drivers of variation in complex gene expression studies. *BMC Bioinformatics* **17**, 483 (2016).

80. Leek, J. T. *et al.* sva: Variable Analysis. *Bioconductor* (2022).

81. Love, M. I., Huber, W. & Anders, S. Moderated estimation of fold change and dispersion for RNA-seq data with DESeq2. *Genome Biol.* **15**, 1–21 (2014).

82. Zhu, A., Ibrahim, J. G. & Love, M. I. Heavy-tailed prior distributions for sequence count data: removing the noise and preserving large differences. *Bioinformatics* **35**, 2084–2092

(2019).

83. Subramanian, A. *et al.* Gene set enrichment analysis: A knowledge-based approach for interpreting genome-wide expression profiles. *Proc. Natl. Acad. Sci.* **102**, 15545–15550 (2005).

84. Ushey, K. & Wickham, H. renv: Project Environments. R package version 1.1.6. (2026).

85. Damiani, C. *et al.* MaREA4Galaxy: Metabolic reaction enrichment analysis and visualization of RNA-seq data within Galaxy. *Comput. Struct. Biotechnol. J.* **18**, 993–999 (2020).

86. Damiani, C. *et al.* A metabolic core model elucidates how enhanced utilization of glucose and glutamine, with enhanced glutamine-dependent lactate production, promotes cancer cell growth: The WarburQ effect. *PLOS Comput. Biol.* **13**, e1005758 (2017).

Figure Captions

Figure 1 **Alterations in *FGFR3* impair lateral cell migration but do not correlate with other functional properties. (a)** Representative images of 2D cultures from bladder cancer cell lines and table resuming classification in terms of staging, grading and presence of alteration of *FGFR3* (cell lines presenting an alteration in *FGFR3* are marked with diagonal lines). Scale bar is 50 µm. **(b)** Growth rate constants of the five UBC cell lines. **(c,d)** Glutathione levels in UBC cell lines: free reduced glutathione (free GSH, c), ratio between free GSH and total glutathione (d). **(e,f)** Representative images of cells stained with DCFDA dye (e) and analysis of intracellular ROS concentration measured as DCFDA intensity per cell (f). Scale bar is 100 µm. **(g,h)** Representative images of cells stained with CellEvent dye (g) and analysis of cell death by apoptosis measured as CellEvent intensity per cell (h). Nuclear staining (Hoechst 33342) is shown in (g) the lower panel for reference of the total cell number. Scale bar is 200 µm. **(i,j)** Representative images of lateral migration (i) and analysis of average migration speed (j). Scale bar is 200 µm. **(k,l)** Representative

images of transwell migration inserts (k) and analysis of transwell migrated cells (l). Scale bar is 1 mm. All the results are shown as mean ± standard deviation. Results are mean of 2-4 experimental replicates and a total of 5-17 technical replicates. Statistical test: ordinary one-way ANOVA, * for $p < 0.05$; ** for $p < 0.01$; *** for $p < 0.001$; **** for $p < 0.0001$.

Figure 2 **Alterations in *FGFR3* correlate with a predominantly oxidative phenotype.** Cell lines presenting an alteration in *FGFR3* are marked with diagonal lines. **(a-h)** Parameters measured using Seahorse technology: basal respiration (a), maximal respiration (b), spare respiratory capacity (c), basal glycolysis (d), maximal glycolysis (e), glycolytic reserve (f), ratio between basal respiration and basal glycolysis (g), ATP production rate index, or ratio between glycoATP and mitoATP production rates (h). **(i)** Unsupervised hierarchical clustering of the five UBC cell lines based on Seahorse data, normalized through UV scaling. Red shades indicate higher-than-average values, while blue shades represent lower-than-average values relative to the dataset mean. White regions correspond to values near the mean. Variables are referred as: BasalR = basal respiration; MaximalR = maximal respiration; MitoATP = ATP produced by mitochondrial respiration; SpareR = spare respiratory capacity; BasalG = basal glycolysis; SpareG = glycolytic reserve; MaximalG = maximal glycolysis; GlycoATP = ATP produced by glycolysis; ATPIndex = GlycoATP/MitoATP. (j) Glycolytic flux measured by imaging analysis using Hylight Biosensor, a fluorescent biosensor for fructose 1,6-bisphosphate (FBP), under baseline condition and after the sequential addition of glucose 10mM, oligomycin 2.5 µM and 2-Deoxy-D-glucose (2-DG) 50 mM. **(k)** Unsupervised hierarchical clustering of the five UBC cell lines based on exometabolomic data, normalized through UV scaling. Red shades indicate higher-than-average values, while blue shades represent lower-than-average values relative to the dataset mean. White regions correspond to exchange rates near the mean. All abbreviations are reported in Supplementary Table 2. **(l-n)** Linear regression analysis between basal respiration from Seahorse technology and glutamine consumption from exometabolomics (l); basal glycolysis from Seahorse technology and glucose consumption from exometabolomics (m); basal glycolysis from Seahorse technology and lactate excretion from exometabolomics (n). All the results are shown as mean ± standard deviation. Results are mean of 7-10 experimental replicates and a total of 80-107 technical replicates (a,d); 2-3 experimental replicates and a total of 8-15 technical replicates (b,c); 5-7 experimental replicates and a total of 41-61 technical replicates (e,f); 3-5 experimental replicates and a total of 18-42 technical replicates (h). Statistical test: ordinary one-way ANOVA, * for $p < 0.05$; ** for $p < 0.01$; *** for $p < 0.001$; **** for $p < 0.0001$.

Figure 3 **Integration of Seahorse and exometabolomic data. (a)** Unsupervised hierarchical clustering of the five UBC cell lines based on their 24 hour-metabolic exchange rates with the medium, four metabolic ratios, and the Seahorse parameters. Unit-Variation scaling was applied to normalize the absolute exchange rates. Red shades indicate higher-than-average exchange rates (either increased consumption or excretion), while blue shades represent lower-than-average exchange rates relative to the dataset mean. White regions correspond to exchange rates near the mean. Metabolites and Seahorse metrics are organized in seven major metabolic clusters. All abbreviations are reported in Supplementary Table 2. **(b)** OPLS-DA score plot of *FGFR3*-alt. (RT112 and J82) and *FGFR3*-wt (5637, UMUC3, and HT1376) UBC cell lines based on 48 metabolite exchange rates, 4 metabolic ratios and 11 Seahorse data. **(c)** Loading plot displaying the contribution of individual metabolites to the group separation. Red markers represent metabolites with VIP > 1. OPLS-DA parameters: A= 1+1+0; N x K= 30 x 64; R2X= 0.484; R2Y= 0.987; Q2= 0.983; CV ANOVA p-value<<0.001.

Figure 4 **Endo-metabolomics analysis corroborates fluxes from Seahorse and exo-metabolomics. (a)** Unsupervised hierarchical clustering of the five UBC cell lines based on endo-metabolomic data. Red shades indicate higher-than-average values, while blue shades represent lower-than-average values relative to the dataset mean. White regions correspond to values near the mean. **(b)** Metabolite enrichment

analysis considering metabolites from endo-metabolomics analysis in the comparison between *FGFR3*-altered vs *FGFR3*-wt cell lines. The analysis shows the 25 most represented metabolite sets, ordered for statistical significance (-log10 of p-value). **(c, d)** Ratios of metabolites, namely glutamate/glutamine (c) and lactate/alanine (d), grouping samples in the comparison *FGFR3*-altered vs *FGFR3*-wt cell lines. All the results are shown as mean ± standard deviation. Results are mean of 2 experimental replicates and a total of 6 technical replicates for each cell line. Statistical test for graphs in panels c and d: unpaired Student's t-test, * for $p < 0.05$.

Figure 5 **Transcriptomic analyses on our UBC cell line panel confirm *FGFR3*-altered BC shift toward oxidative metabolism. (a)** Gene Set Enrichment Analysis (GSEA) on transcriptomic data using the 50 Hallmark gene sets. Significative gene sets were selected for an FDR q-val < 5% and ordered for Normalized Enrichment Score (NES). **(b)** Map representing fluxes' prediction of main metabolic reactions using ENGRO2 model[47,48]. Purple and yellow arrows represent respectively down-regulated and up-regulated reactions in the *FGFR3*-altered compared to the *FGFR3*-wt group, setting fold change > 1.2 and p-value < 0.05 as thresholds.

Figure 6 **A computational analysis performed on transcriptomic data from the BC patient's dataset (TCGA, Cell 2017) corroborates experimental results on cell lines. (a)** Gene Set Enrichment Analysis (GSEA) on transcriptomic data using the 50 Hallmark gene sets. Significative gene sets were selected for an FDR q-val < 5% and ordered for Normalized Enrichment Score (NES). **(b)** Mapping of RASs using ENGRO2 model[47,48]. Purple and yellow arrows represent respectively down-regulated and up-regulated reactions in the *FGFR3*-altered compared to the *FGFR3*-wt group, setting z-score > 0.5 and p-value < 0.05 as thresholds.

Figure 7 **FGFR3 and OXPHOS pharmacological inhibition in UBC cell lines. (a, b)** Viable cell number (a, cell count at t0=1) and cell mortality (b, vehicle mortality=0) and cell mortality (g, showed as vehicle mortality=0) after 72h of treatment with increasing concentrations of FGFR3 inhibitor Erdafitinib (0.5, 5, 50, 500 nM). **(c-e)** Respiratory parameters measured through Seahorse analysis on cells after 24h of treatment with increasing concentrations of Erdafitinib (0.5, 5, 50, 500 nM). Basal respiration (c, vehicle=1), maximal respiration (d, vehicle=1), ATP-linked respiration (e, vehicle=1). **(f, g)** Viable cell number (f, cell count at t0=1) and cell mortality (g, vehicle mortality=0) after 72h of treatment with increasing concentrations of ETC complex I inhibitor IACS-010759 (0.5, 5, 50, 500 nM). All the results are shown as mean ± standard deviation. Results are mean of 2-3 experimental replicates and a total of 6-9 technical replicates. Statistical test: ordinary two-way ANOVA (a,b,f,g), ordinary one-way ANOVA (c-e), * for $p < 0.05$; ** for $p < 0.01$; *** for $p < 0.001$; **** for $p < 0.0001$.

Editor Summary

A multi-omics study demonstrates that FGFR3 oncogenic activation drives oxidative metabolic reprogramming in bladder cancer. These findings highlight a vulnerability to mitochondrial inhibitors as a precision therapy for FGFR3-altered tumours.

Peer Review Information

Communications Biology thanks Philip Abbosh and He Wen for their contribution to the peer review of this work. Primary Handling Editors: Kaliya Georgieva. A peer review file is available.

Experimental model

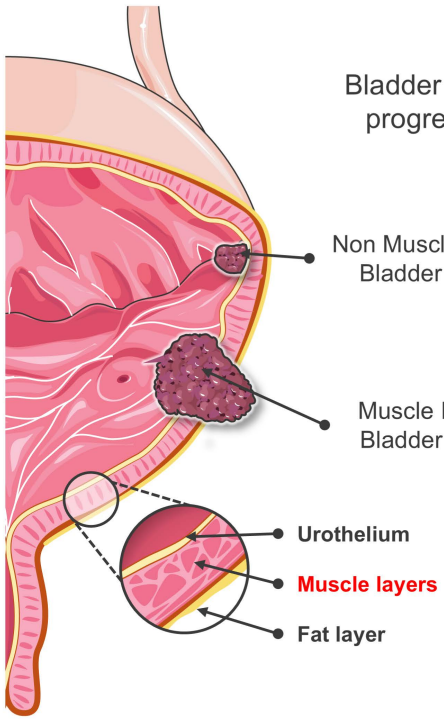

Bladder cancer progression

Non Muscle Invasive Bladder Cancer

Muscle Invasive Bladder Cancer

BC cell line panel

NMIBC: RT112

MIBC: 5637, UMUC3, HT1376, J82

***FGFR3* condition**

***FGFR3*-altered**

***FGFR3*-wt**

***FGFR3*-altered**

Publicly available cell line and MIBC patients' datasets

Transcriptomic data from **CCLE** and **TCGA (Cell, 2017)**

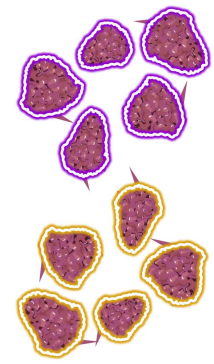

***FGFR3*-wt MIBCs**

***FGFR3*-alt. MIBCs**

Data integration

Multi-omics systems metabolomics approach

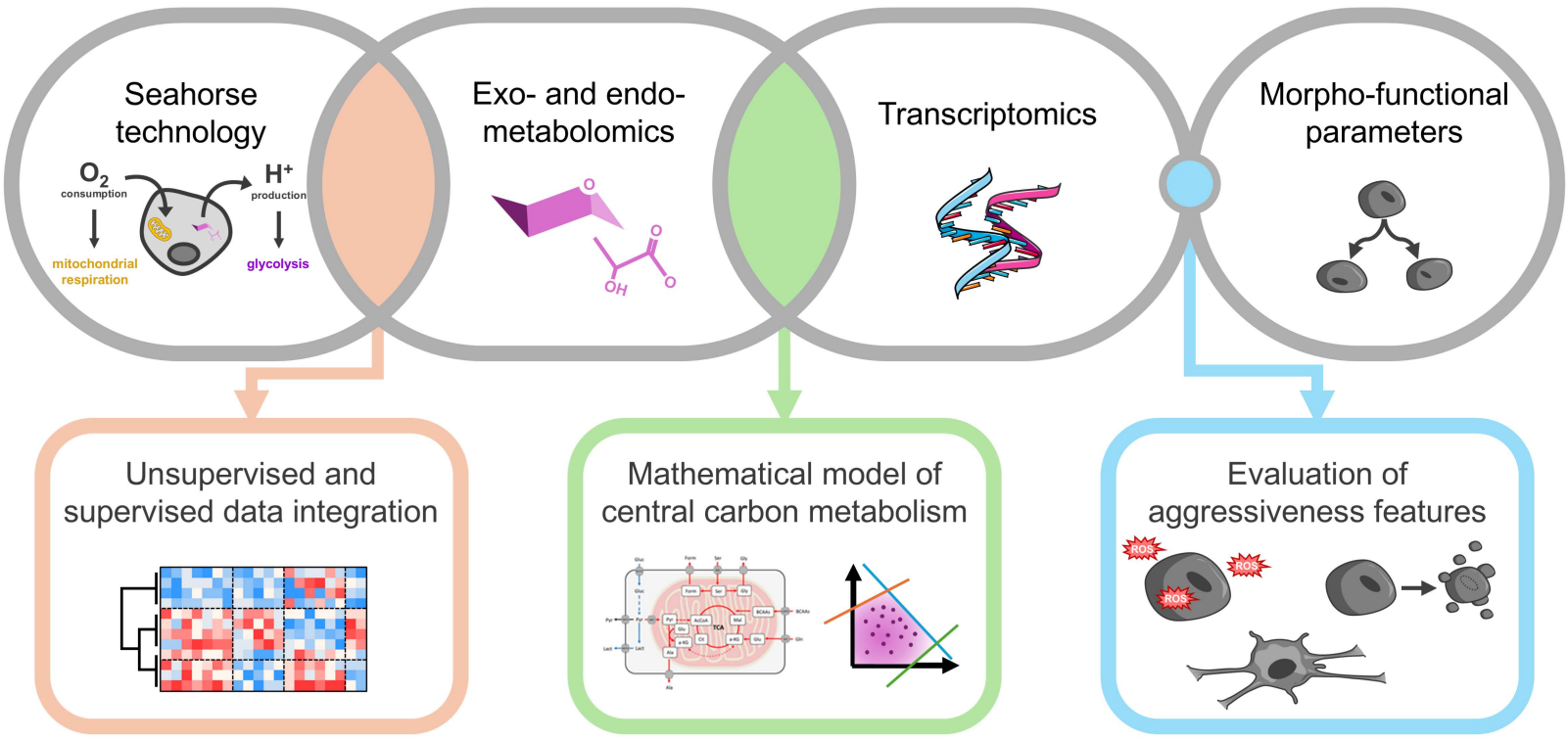

Results

Predominantly oxidative, poorly migratory phenotype in *FGFR3*-altered samples

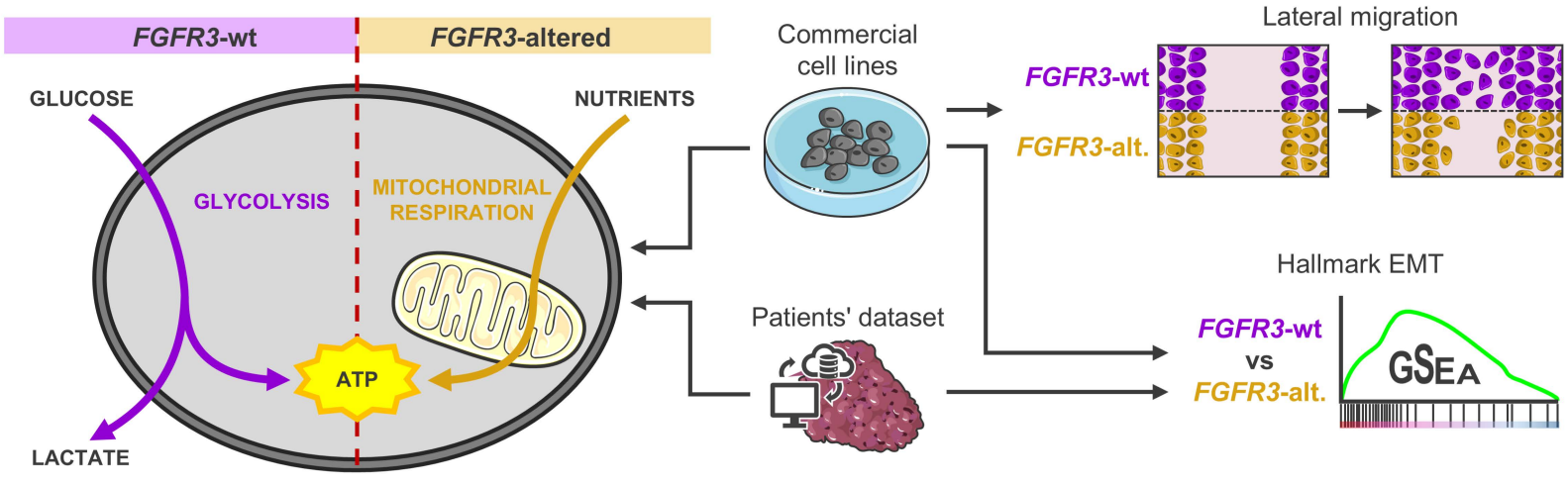

OXPHOS targeting in *FGFR3*-altered samples

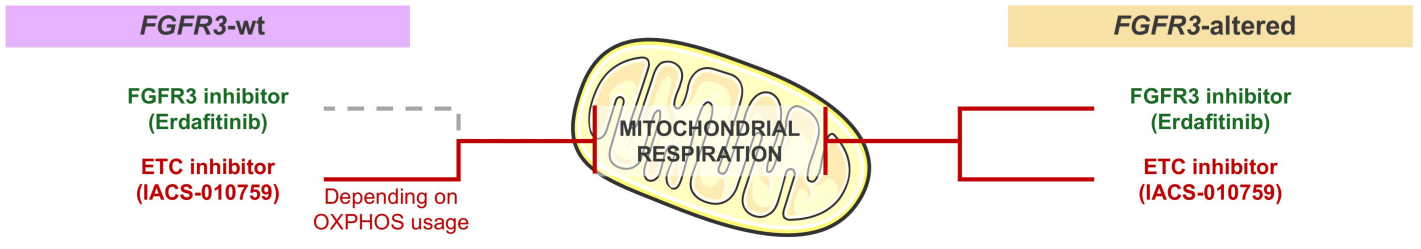

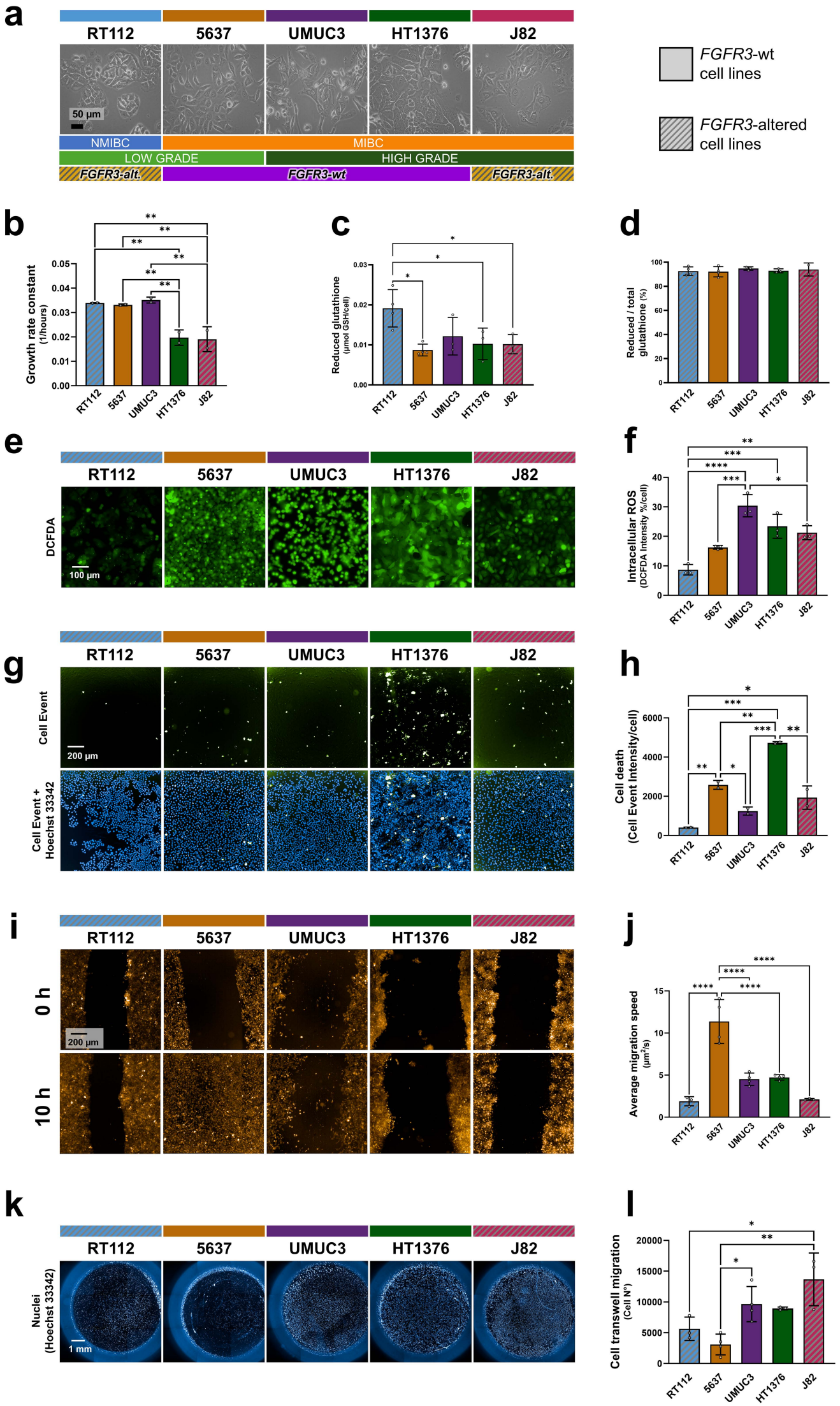
a
RT112
5637
UMUC3
HT1376
J82
50 µm
NMIBC
MIBC
LOW GRADE
HIGH GRADE
FGFR3-alt.
FGFR3-wt
FGFR3-alt.
FGFR3-wt cell lines
FGFR3-altered cell lines
b
Growth rate constant (1/hours)
c
Reduced glutathione (µmol GSH/cell)
d
Reduced / total glutathione (%)
e
DCFDA
100 µm
f
Intracellular ROS (DCFDA Intensity %/cell)
g
Cell Event
Cell Event + Hoechst 33342
200 µm
h
Cell death (Cell Event Intensity/cell)
i
0 h
10 h
200 µm
j
Average migration speed (µm²/s)
k
Nuclei (Hoechst 33342)
1 mm
l
Cell transwell migration (Cell N°)

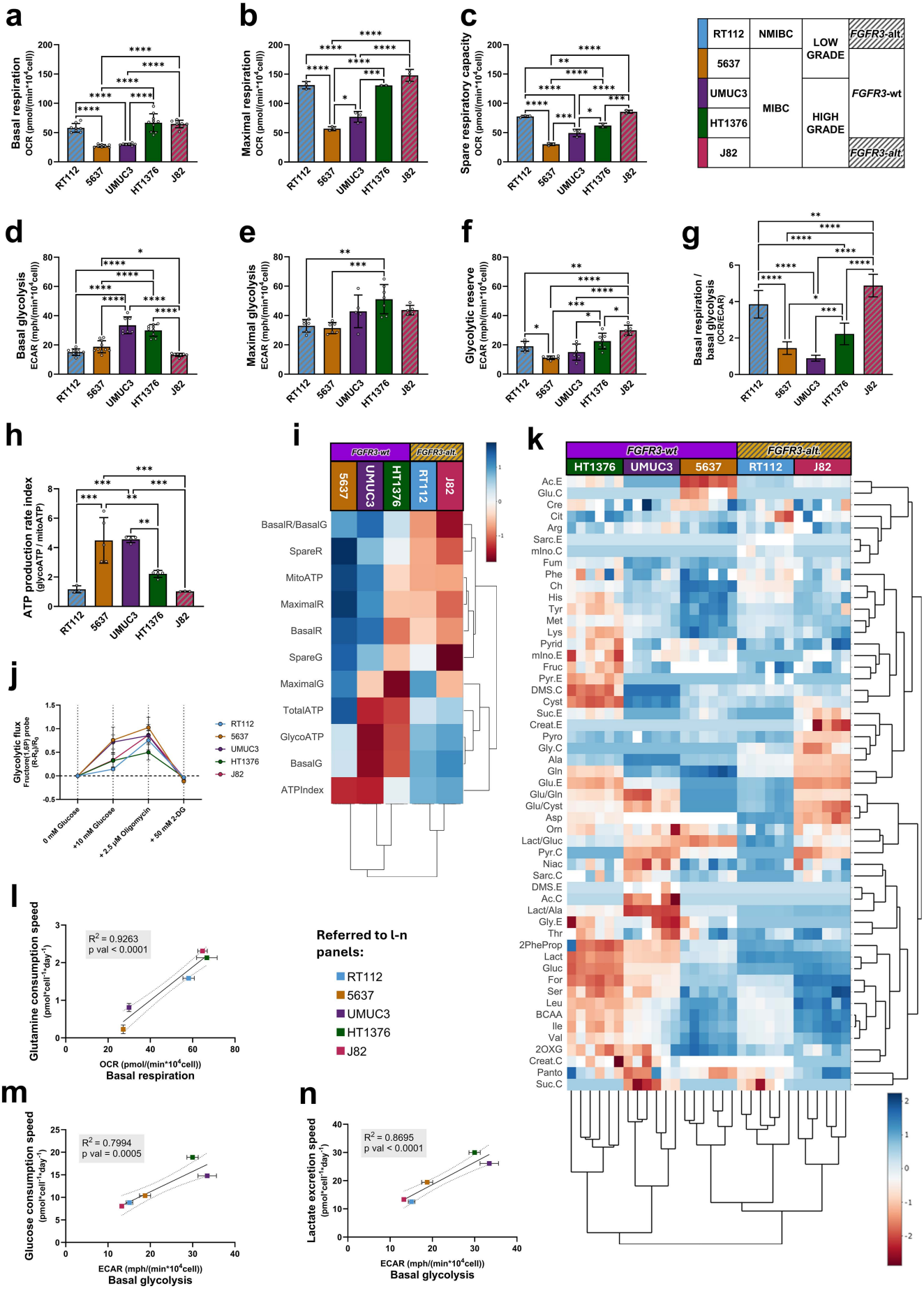
a
Basal respiration
OCR (pmol/(min*10^4cell))
b
Maximal respiration
OCR (pmol/(min*10^4cell))
c
Spare respiratory capacity
OCR (pmol/(min*10^4cell))
RT112
5637
UMUC3
HT1376
J82
NMIBC
MIBC
LOW GRADE
HIGH GRADE
FGFR3-alt.
FGFR3-wt
d
Basal glycolysis
ECAR (mph/(min*10^4cell))
e
Maximal glycolysis
ECAR (mph/(min*10^4cell))
f
Glycolytic reserve
ECAR (mph/(min*10^4cell))
g
Basal respiration / basal glycolysis
(OCR/ECAR)
h
ATP production rate index
(glycoATP / mitoATP)
i
FGFR3-wt
FGFR3-alt.
BasalR/BasalG
SpareR
MitoATP
MaximalR
BasalR
SpareG
MaximalG
TotalATP
GlycoATP
BasalG
ATPIndex
k
Ac.E
Glu.C
Cre
Cit
Arg
Sarc.E
mIno.C
Fum
Phe
Ch
His
Tyr
Met
Lys
Pyrid
mIno.E
Fruc
Pyr.E
DMS.C
Cyst
Suc.E
Creat.E
Pyro
Gly.C
Ala
Gln
Glu.E
Glu/Gln
Glu/Cyst
Asp
Orn
Lact/Gluc
Pyr.C
Niac
Sarc.C
DMS.E
Ac.C
Lact/Ala
Gly.E
Thr
2PheProp
Lact
Gluc
For
Ser
Leu
BCAA
Ile
Val
2OXG
Creat.C
Panto
Suc.C
j
Glycolytic flux
Fructose1,6P1 probe
(R-R0)/R0
0 mM Glucose
+10 mM Glucose
+ 2.5 µM Oligomycin
+ 50 mM 2-DG
l
Glutamine consumption speed
(pmol*cell^-1*day^-1)
R2 = 0.9263
p val < 0.0001
OCR (pmol/(min*10^4cell))
Basal respiration
Referred to l-n panels:
m
Glucose consumption speed
(pmol*cell^-1*day^-1)
R2 = 0.7994
p val = 0.0005
ECAR (mph/(min*10^4cell))
Basal glycolysis
n
Lactate excretion speed
(pmol*cell^-1*day^-1)
R2 = 0.8695
p val < 0.0001
ECAR (mph/(min*10^4cell))
Basal glycolysis

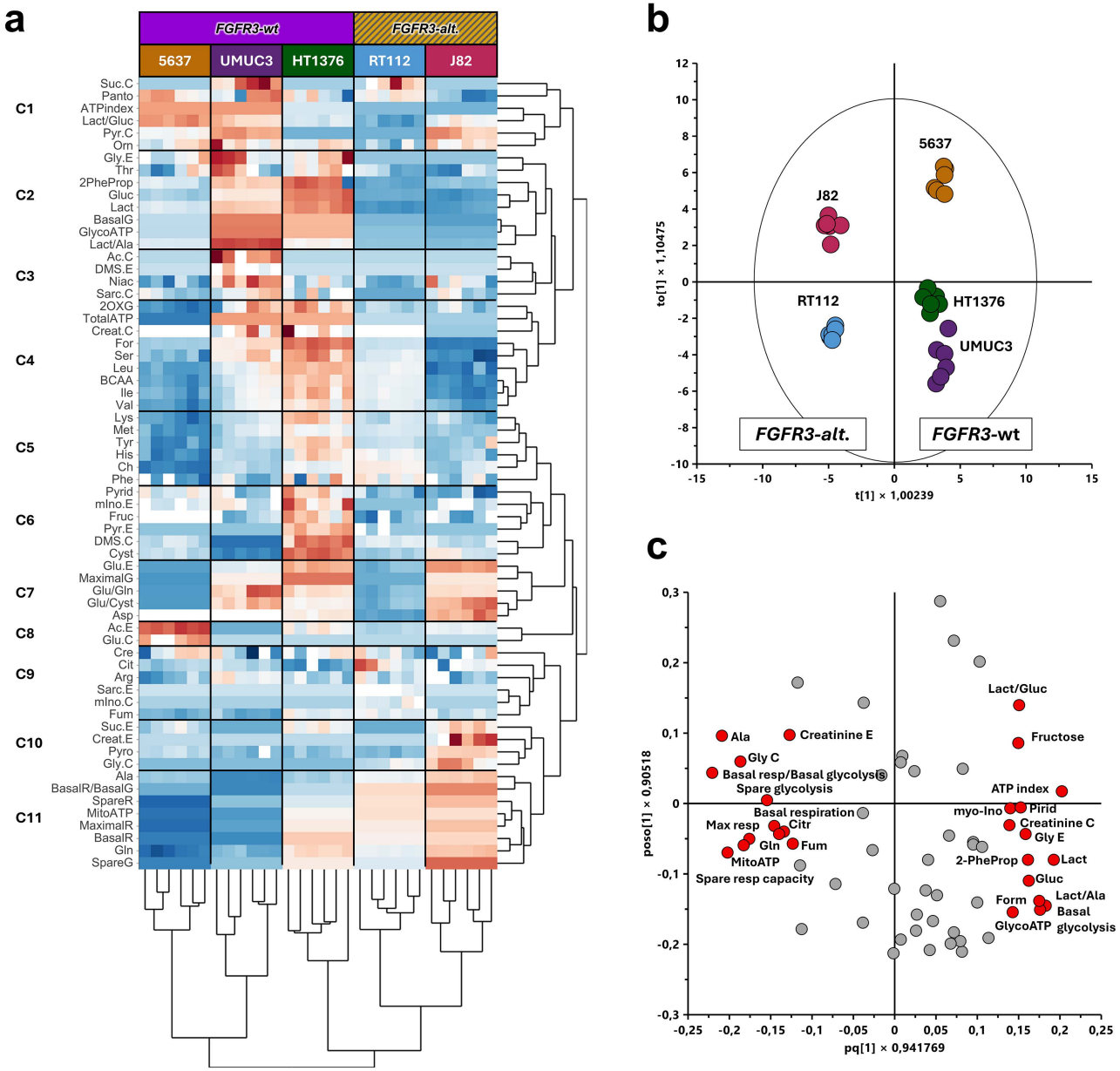
a
FGFR3-wt
FGFR3-alt.
5637
UMUC3
HT1376
RT112
J82
C1
Suc.C
Panto
ATPindex
Lact/Gluc
Pyr.C
Orn
C2
Gly.E
Thr
2PheProp
Gluc
Lact
BasalG
GlycoATP
Lact/Ala
C3
Ac.C
DMS.E
Niac
Sarc.C
C4
2OXG
TotalATP
Creat.C
For
Ser
Leu
BCAA
Ile
Val
C5
Lys
Met
Tyr
His
Ch
Phe
C6
Pyrid
mIno.E
Fruc
Pyr.E
DMS.C
Cyst
C7
Glu.E
MaximalG
Glu/Gln
Glu/Cyst
Asp
C8
Ac.E
Glu.C
Cre
C9
Cit
Arg
Sarc.E
mIno.C
Fum
C10
Suc.E
Creat.E
Pyro
Gly.C
Ala
C11
BasalR/BasalG
SpareR
MitoATP
MaximalR
BasalR
Gln
SpareG
b
5637
J82
RT112
HT1376
UMUC3
FGFR3-alt.
FGFR3-wt
to[1] × 1,10475
t[1] × 1,00239
c
Lact/Gluc
Ala
Creatinine E
Fructose
Gly C
Basal resp/Basal glycolysis
Spare glycolysis
ATP index
Basal respiration
myo-Ino
Pirid
Max resp
Citr
Creatinine C
Gly E
Gln
Fum
2-PheProp
Lact
MitoATP
Gluc
Spare resp capacity
Form
Lact/Ala
Basal
GlycoATP
glycolysis
poso[1] × 0,90518
pq[1] × 0,941769

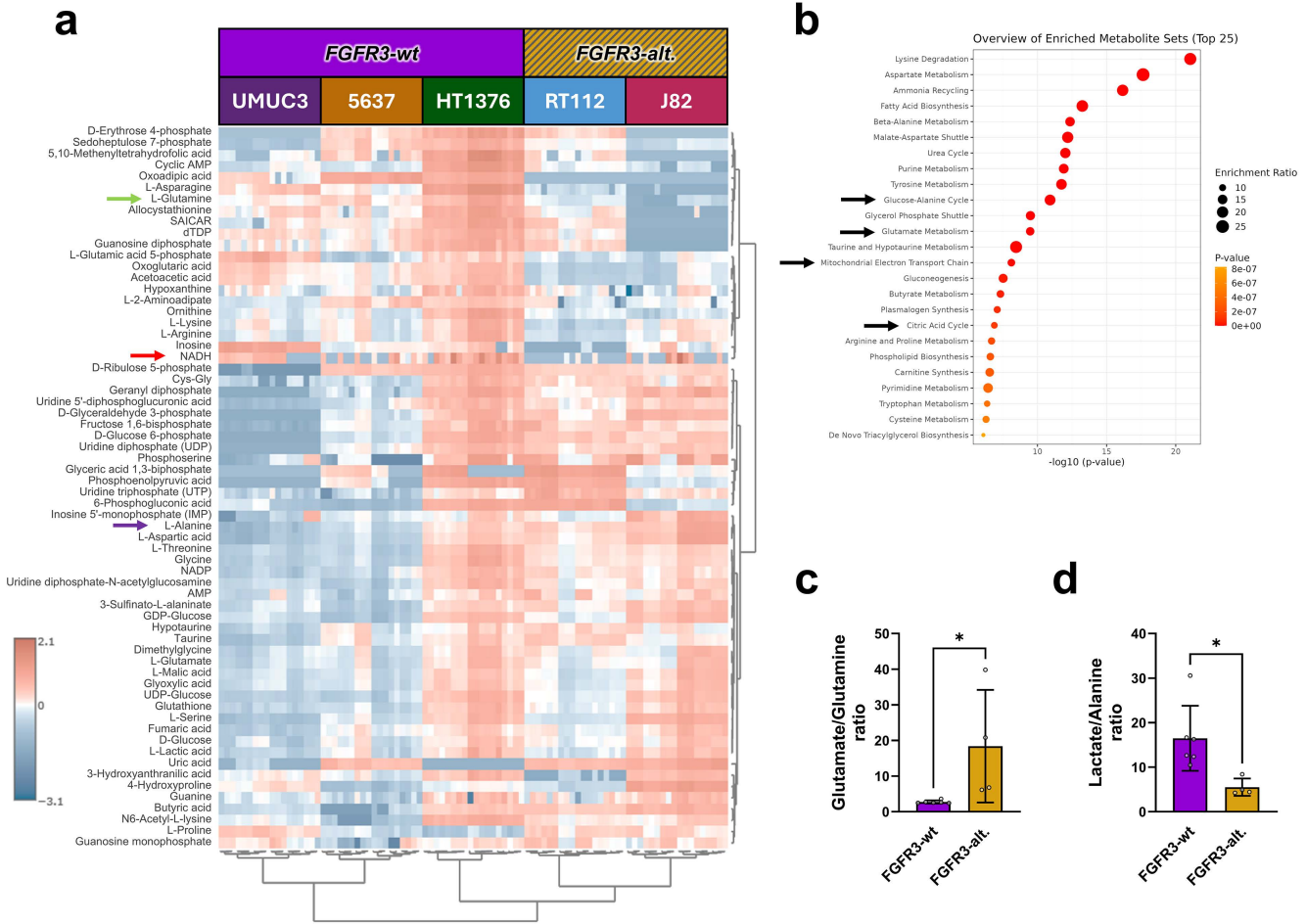
a
FGFR3-wt
FGFR3-alt.
UMUC3
5637
HT1376
RT112
J82
D-Erythrose 4-phosphate
Sedoheptulose 7-phosphate
5,10-Methenyltetrahydrofolic acid
Cyclic AMP
Oxoadipic acid
L-Asparagine
L-Glutamine
Allocystathionine
SAICAR
dTDP
Guanosine diphosphate
L-Glutamic acid 5-phosphate
Oxoglutaric acid
Acetoacetic acid
Hypoxanthine
L-2-Aminoadipate
Ornithine
L-Lysine
L-Arginine
Inosine
NADH
D-Ribulose 5-phosphate
Cys-Gly
Geranyl diphosphate
Uridine 5'-diphosphoglucuronic acid
D-Glyceraldehyde 3-phosphate
Fructose 1,6-bisphosphate
D-Glucose 6-phosphate
Uridine diphosphate (UDP)
Phosphoserine
Glyceric acid 1,3-biphosphate
Phosphoenolpyruvic acid
Uridine triphosphate (UTP)
6-Phosphogluconic acid
Inosine 5'-monophosphate (IMP)
L-Alanine
L-Aspartic acid
L-Threonine
Glycine
NADP
Uridine diphosphate-N-acetylglucosamine
AMP
3-Sulfinato-L-alaninate
GDP-Glucose
Hypotaurine
Taurine
Dimethylglycine
L-Glutamate
L-Malic acid
Glyoxylic acid
UDP-Glucose
Glutathione
L-Serine
Fumaric acid
D-Glucose
L-Lactic acid
Uric acid
3-Hydroxyanthranilic acid
4-Hydroxyproline
Guanine
Butyric acid
N6-Acetyl-L-lysine
L-Proline
Guanosine monophosphate
2.1
0
−3.1
b
Overview of Enriched Metabolite Sets (Top 25)
Lysine Degradation
Aspartate Metabolism
Ammonia Recycling
Fatty Acid Biosynthesis
Beta-Alanine Metabolism
Malate-Aspartate Shuttle
Urea Cycle
Purine Metabolism
Tyrosine Metabolism
Glucose-Alanine Cycle
Glycerol Phosphate Shuttle
Glutamate Metabolism
Taurine and Hypotaurine Metabolism
Mitochondrial Electron Transport Chain
Gluconeogenesis
Butyrate Metabolism
Plasmalogen Synthesis
Citric Acid Cycle
Arginine and Proline Metabolism
Phospholipid Biosynthesis
Carnitine Synthesis
Pyrimidine Metabolism
Tryptophan Metabolism
Cysteine Metabolism
De Novo Triacylglycerol Biosynthesis
10
15
20
-log10 (p-value)
Enrichment Ratio
10
15
20
25
P-value
8e-07
6e-07
4e-07
2e-07
0e+00
c
Glutamate/Glutamine ratio
50
40
30
20
10
0
*
FGFR3-wt
FGFR3-alt.
d
Lactate/Alanine ratio
40
30
20
10
0
*
FGFR3-wt
FGFR3-alt.

a

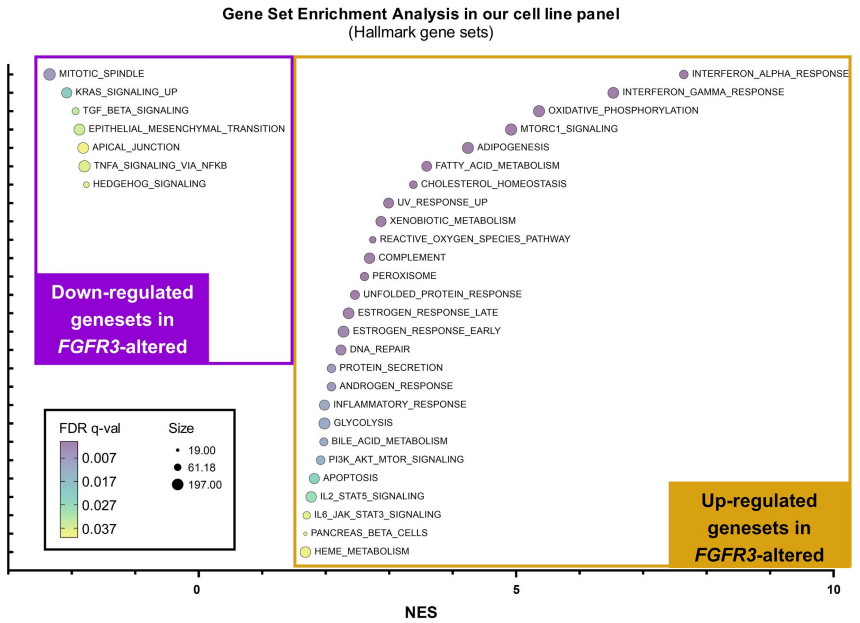
Gene Set Enrichment Analysis in our cell line panel
(Hallmark gene sets)
MITOTIC_SPINDLE
KRAS_SIGNALING_UP
TGF_BETA_SIGNALING
EPITHELIAL_MESENCHYMAL_TRANSITION
APICAL_JUNCTION
TNFA_SIGNALING_VIA_NFKB
HEDGEHOG_SIGNALING
Down-regulated genesets in FGFR3-altered
INTERFERON_ALPHA_RESPONSE
INTERFERON_GAMMA_RESPONSE
OXIDATIVE_PHOSPHORYLATION
MTORC1_SIGNALING
ADIPOGENESIS
FATTY_ACID_METABOLISM
CHOLESTEROL_HOMEOSTASIS
UV_RESPONSE_UP
XENOBIOTIC_METABOLISM
REACTIVE_OXYGEN_SPECIES_PATHWAY
COMPLEMENT
PEROXISOME
UNFOLDED_PROTEIN_RESPONSE
ESTROGEN_RESPONSE_LATE
ESTROGEN_RESPONSE_EARLY
DNA_REPAIR
PROTEIN_SECRETION
ANDROGEN_RESPONSE
INFLAMMATORY_RESPONSE
GLYCOLYSIS
BILE_ACID_METABOLISM
PI3K_AKT_MTOR_SIGNALING
APOPTOSIS
IL2_STAT5_SIGNALING
IL6_JAK_STAT3_SIGNALING
PANCREAS_BETA_CELLS
HEME_METABOLISM
Up-regulated genesets in FGFR3-altered
FDR q-val
0.007
0.017
0.027
0.037
Size
19.00
61.18
197.00
0
5
10
NES

b

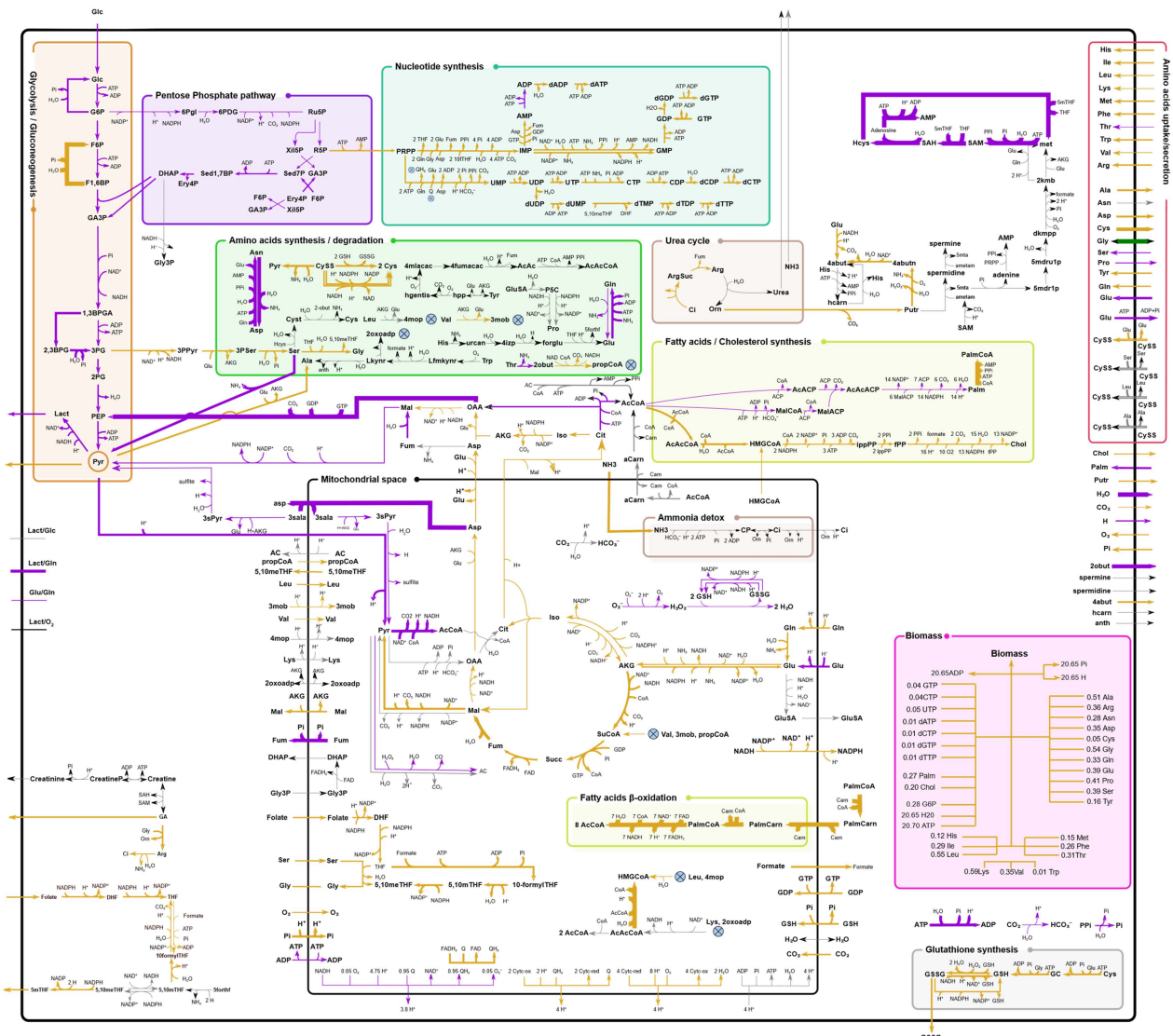
Glycolysis / Gluconeogenesis
Pentose Phosphate pathway
Nucleotide synthesis
Amino acids synthesis / degradation
Urea cycle
Fatty acids / Cholesterol synthesis
Mitochondrial space
Ammonia detox
Fatty acids β-oxidation
Biomass
Glutathione synthesis
Amino acids uptake/secretion
Lact/Glc
Lact/Gln
Glu/Gln
Lact/O2
= Down-regulated in FGFR3-altered
= Up-regulated in FGFR3-altered
= From backward to forward in FGFR3-altered
= From forward to backward in FGFR3-altered
Arrow thickness is proportional to z-score

a

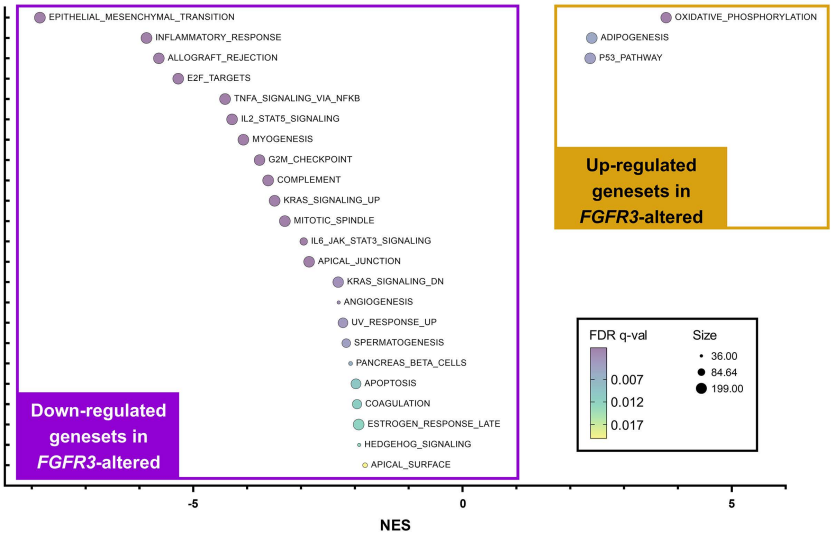
Gene Set Enrichment Analysis in TCGA_2017 patient dataset
(Hallmark gene sets)
EPITHELIAL_MESENCHYMAL_TRANSITION
INFLAMMATORY_RESPONSE
ALLOGRAFT_REJECTION
E2F_TARGETS
TNFA_SIGNALING_VIA_NFKB
IL2_STAT5_SIGNALING
MYOGENESIS
G2M_CHECKPOINT
COMPLEMENT
KRAS_SIGNALING_UP
MITOTIC_SPINDLE
IL6_JAK_STAT3_SIGNALING
APICAL_JUNCTION
KRAS_SIGNALING_DN
ANGIOGENESIS
UV_RESPONSE_UP
SPERMATOGENESIS
PANCREAS_BETA_CELLS
APOPTOSIS
COAGULATION
ESTROGEN_RESPONSE_LATE
HEDGEHOG_SIGNALING
APICAL_SURFACE
OXIDATIVE_PHOSPHORYLATION
ADIPOGENESIS
P53_PATHWAY
Up-regulated genesets in FGFR3-altered
Down-regulated genesets in FGFR3-altered
FDR q-val
0.007
0.012
0.017
Size
36.00
84.64
199.00
-5
0
5
NES

b

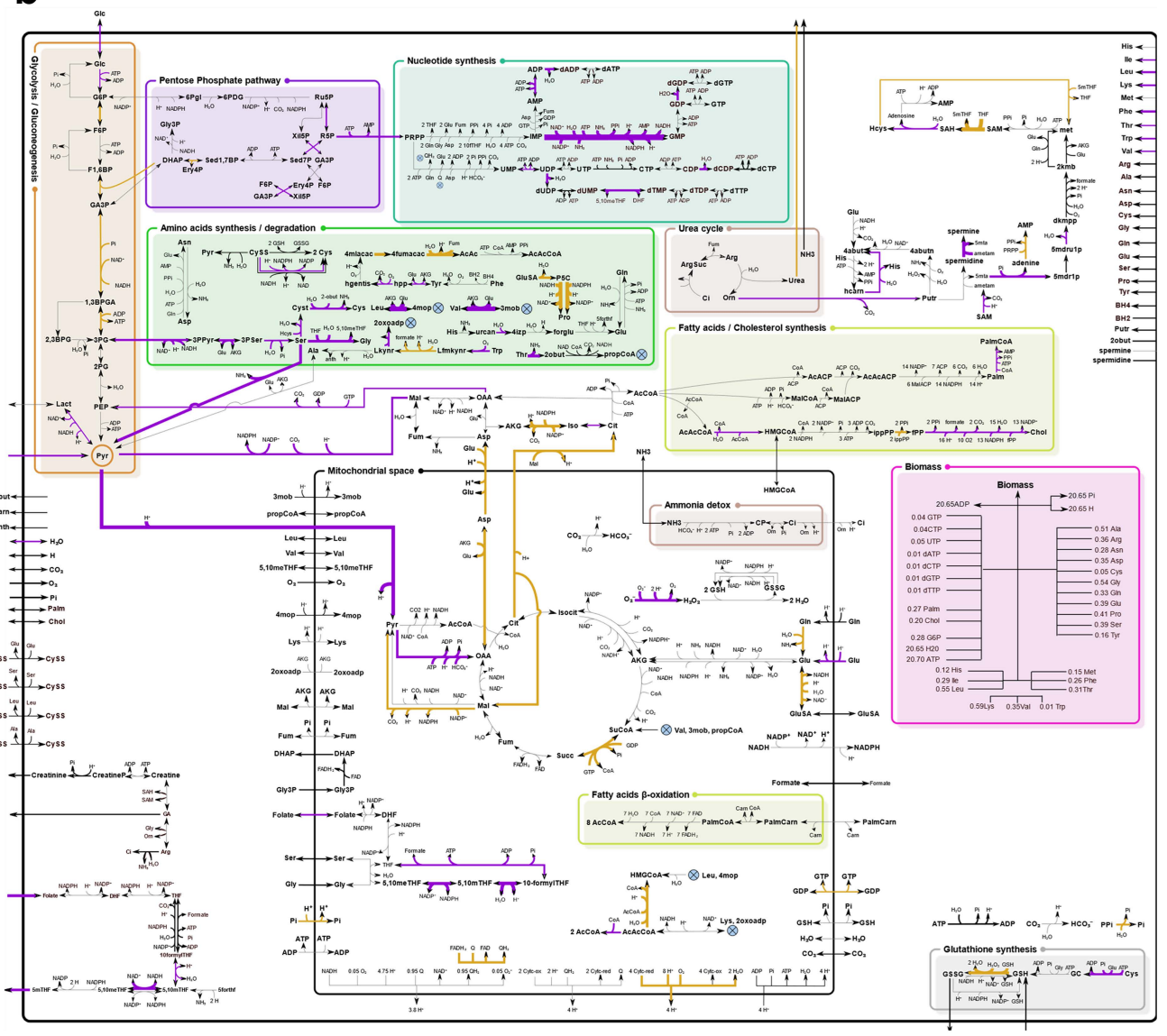
Glycolysis / Gluconeogenesis
Pentose Phosphate pathway
Nucleotide synthesis
Amino acids synthesis / degradation
Urea cycle
Fatty acids / Cholesterol synthesis
Mitochondrial space
Ammonia detox
Fatty acids β-oxidation
Biomass
Glutathione synthesis
= Down-regulated in FGFR3-altered
= Up-regulated in FGFR3-altered
Arrow thickness is proportional to z-score

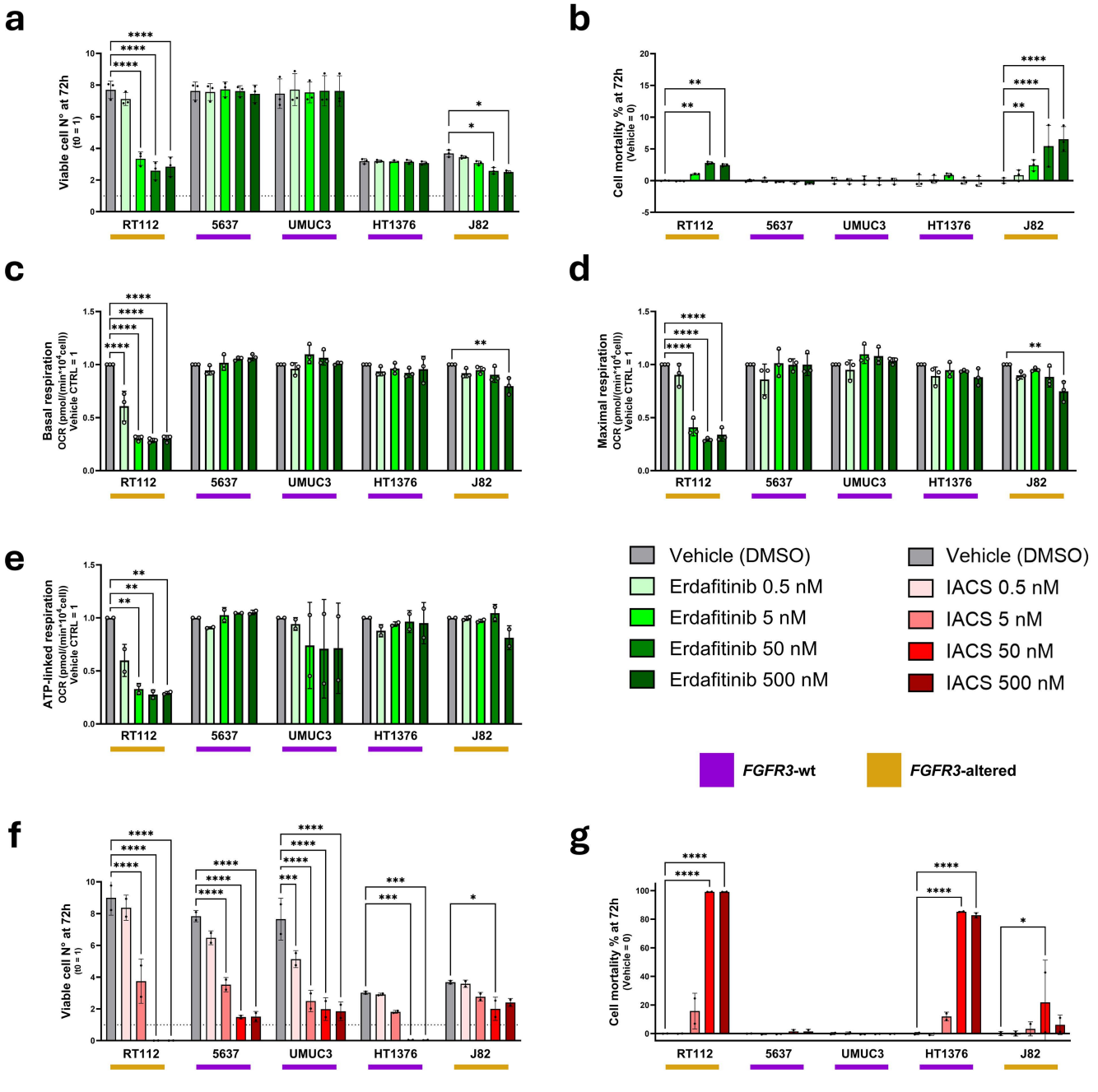
a
Viable cell N° at 72h
(t0 = 1)
b
Cell mortality % at 72h
(Vehicle = 0)
c
Basal respiration
OCR (pmol/(min*10⁴cell))
Vehicle CTRL = 1
d
Maximal respiration
OCR (pmol/(min*10⁴cell))
Vehicle CTRL = 1
e
ATP-linked respiration
OCR (pmol/(min*10⁴cell))
Vehicle CTRL = 1
RT112
5637
UMUC3
HT1376
J82
Vehicle (DMSO)
Erdafitinib 0.5 nM
Erdafitinib 5 nM
Erdafitinib 50 nM
Erdafitinib 500 nM
Vehicle (DMSO)
IACS 0.5 nM
IACS 5 nM
IACS 50 nM
IACS 500 nM
FGFR3-wt
FGFR3-altered
f
Viable cell N° at 72h
(t0 = 1)
g
Cell mortality % at 72h
(Vehicle = 0)